Angular anisotropy of secondary neutron spectra in ^{232}Th+n
&
Anisotropy of prompt fission neutron spectra of ^{235}U(n,F)

Vladimir Maslov
220025, Minsk, Byelorussia

29th International Seminar on Interaction of Neutrons with Nuclei: May 29 - June 2, 2023, Frank' LNP, JINR, Dubna, Russia

Collaboration on PFNS of 2000-2011

- *V.M. Maslov[1] , Yu. V. Porodzinskij[1], N.A. Tetereva[1],*
- *A.B. Kagalenko[2], N.V. Kornilov[2], V.P.Pronyaev[2],*
- *M. Baba[3], A. Hasegawa[4],*
- *T. Granier[5], F.-J. Hambsch[6]*
- [1] JINER, Minsk-Sosny, Byelorussia
- [2] Institute of Physics and Power Engineering, Obninsk, Russia
- [3] Tohoku University, Sendai, Japan
- [4] JAEA, Tokai-mura, Japan
- [5] CEA, Centre DAM-Ile de France, 91927,Arpajon, Cedex, France
- [6] EU-JRC Institute for Reference Materials and Measurements, Geel, Belgium

PHYSICAL REVIEW LETTERS 122, 072503 (2019)

Preequilibrium Asymmetries in the ^{239}Pu(n,f) Prompt Fission Neutron Spectrum

K. J. Kelly,[1,*] T. Kawano,[1] J. M. O'Donnell,[1] J. A. Gomez,[1] M. Devlin,[1] D. Neudecker,[1] P. Talou,[1] A. E. Lovell,[1] M. C. White,[1] R. C. Haight,[1] T. N. Taddeucci,[1] S. M. Mosby,[1] H. Y. Lee,[1] C. Y. Wu,[2] R. Henderson,[2] J. Henderson,[2] and M. Q. Buckner[2]

[1]*Los Alamos National Laboratory, Los Alamos, New Mexico 87545, USA*
[2]*Lawrence Livermore National Laboratory, Livermore, California 94550, USA*

(Received 10 December 2018; revised manuscript received 9 January 2019; published 22 February 2019)

The physical properties of neutrons emitted from neutron-induced fission are fundamental to our understanding of nuclear fission. However, while state-of-the-art fission models still incorporate isotropic fission neutron spectra, it is believed that the preequilibrium prefission component of these spectra is strongly anisotropic. The lack of experimental guidance on this feature has not motivated incorporation of anisotropic neutron spectra in fission models, though any significant anisotropy would impact descriptions

Phys. Rev. Lett. V. 122,072503 (2019)

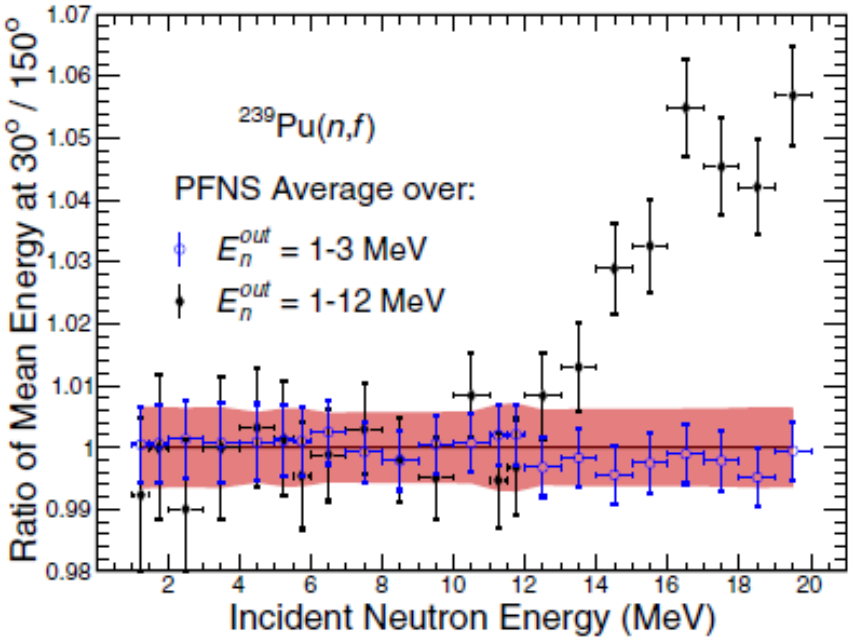

FIG. 4. The ratios of the average PFNS energy over an outgoing range of $E_n^{\text{out}} = 1$–3 MeV (blue open circles) and $E_n^{\text{out}} = 1$–12 MeV (black diamonds) at a detection angle of 30° to the same quantity calculated at 150° as a function of incident neutron energy are shown. The uncertainties on the data points represent the uncertainty on the mean energy at 30°, while the width of the shaded region around a ratio of unity (red online) represents the uncertainty of the mean energy at 150° for $E_n^{\text{out}} = 1$–12 MeV. See the text for discussion.

- **Asymmetry in neutron emission spectra E_n=14 MeV**

•235-U+n; 239-Pu+n; 238-U+n – first observed by

- Kammerdiener J.L., UCRL-51232, **1972**.
- **Asymmetry of pre-fission neutron emission in**
- **239-Pu(n,F) Prompt Fission Neutron Spectra by**
- Kelly e. a., Phys. Rev. Lett., **2019**, v. 122, p. 072503
- **Asymmetry in neutron emission spectra of 232Th+n at E_n = 2-18 MeV first observed by**
- M. Baba et al., JAERI-M-89-143, **1989**
- **Asymmetry of pre-fission neutron emission in 232Th(n,F) PFNS ???**

Asymmetry of pre-fission neutron emission in 235-U(n,F) vis 239-Pu(n,F)

Angular anisotropy (AA) of secondary neutrons is evidenced in neutron emission spectra (NES) due to

1. (n,n)
2. **g.s. band levels** $J^{\pi}= 0^{+}, 2^{+}, 4^{+}, 6^{+}, 8^{+}$ (e-e)
3. γ–bands with $K^{\pi}=0^{+}, 2^{+}$, octupole bands $K^{\pi}=0^{-}$ (e-e)
4. (n,nγ)

NES **AA** is due to PE/semi-direct $(n,nX)^{1}$

Angular anisotropy of PFNS due to tiny part of $(n,nX)^{1}$ neutrons in exclusive pre-fission neutrons in $(n,xnf)^{1,\ldots,x}$.

Available online at www.sciencedirect.com
SCIENCE DIRECT®
Nuclear Physics A 764 (2006) 212–245
NUCLEAR PHYSICS A

Excitation of octupole, beta- and gamma-vibration band levels of ^{238}U by inelastic neutron scattering

V.M. Maslov [a,*], Yu.V. Porodzinskij [a], N.A. Tetereva [a], M. Baba [b], A. Hasegawa [c]

[a] Joint Institute for Nuclear and Energy Research, 220109 Minsk-Sosny, Belarus
[b] Cyclotron and Radioisotope Center, Tohoku University, Sendai, Japan
[c] Research Establishment, Japan Atomic Energy Research Institute, Tokai-mura, Naka-gun, Ibaraki-ken, Japan

Received 20 March 2003; received in revised form 8 August 2005; accepted 29 September 2005

Available online 12 October 2005

Abstract

Experimental data on inelastic neutron scattering are analyzed in a Hauser–Feshbach–Moldauer approach with a coupled-channel estimates of the direct reaction contribution. For the direct excitation of the ground state rotational band levels with $J^\pi = 0^+, 2^+, 4^+, 6^+, 8^+$ the rigid rotator model was used, whereas for the direct excitation of members of the β-, γ- ($K^\pi = 0_2^+, 0_3^+, 2^+$) and first octupole band ($K^\pi = 0^-$) a soft-deformable rotator model was used. Quadrupole, octupole, hexadecapole and gamma-deformation parameters are defined by consistent analysis of excited rotational–vibrational band structures and excitation cross sections of the relevant levels. Structures evident in measured neutron emission spectra for $E_n \sim$ 1–6 MeV are correlated with excitation of levels of $K^\pi = 0^-$ and $K^\pi = 0_2^+, 0_3^+, 2^+$ bands.

V. M. Maslov, e.a. INDC(BLR)-16, IAEA, Vienna (2003),
https://www-nds.iaea.org/publications/indc/indc-blr-0016/
V. M. Maslov, e.a. 232Th evaluated data file https://www-nds.iaea.org/minskact

Table 6
Coupling scheme for ^{232}Th

			1.1483; 4^+	
		1.1460; 7^+		
			1.1218; 2^+	
			1.0787; 0^+	
		1.0499; 6^+		
	1.0429; 7^-			
				1.0231; 6^+
				0.9604; 5^+
		0.8901; 4^+		
	0.8836; 5^-			
				0.8730; 4^+
				0.8296; 3^+
				0.7853; 2^+
	0.7744; 3^-			
		0.7741; 2^+		
		0.7303; 0^+		
	0.71425; 1^-			
0.3332; 6^+				
0.16212; 4^+				
0.049369; 2^+				
0.0000; 0^+		n_β=1	n_γ=1	
$K^\pi = 0^+$	$K^\pi = 1^-$	$K^\pi = 0^+$	$K^\pi = 0^+$	$K^\pi = 2^+$

6 MeV 30 deg

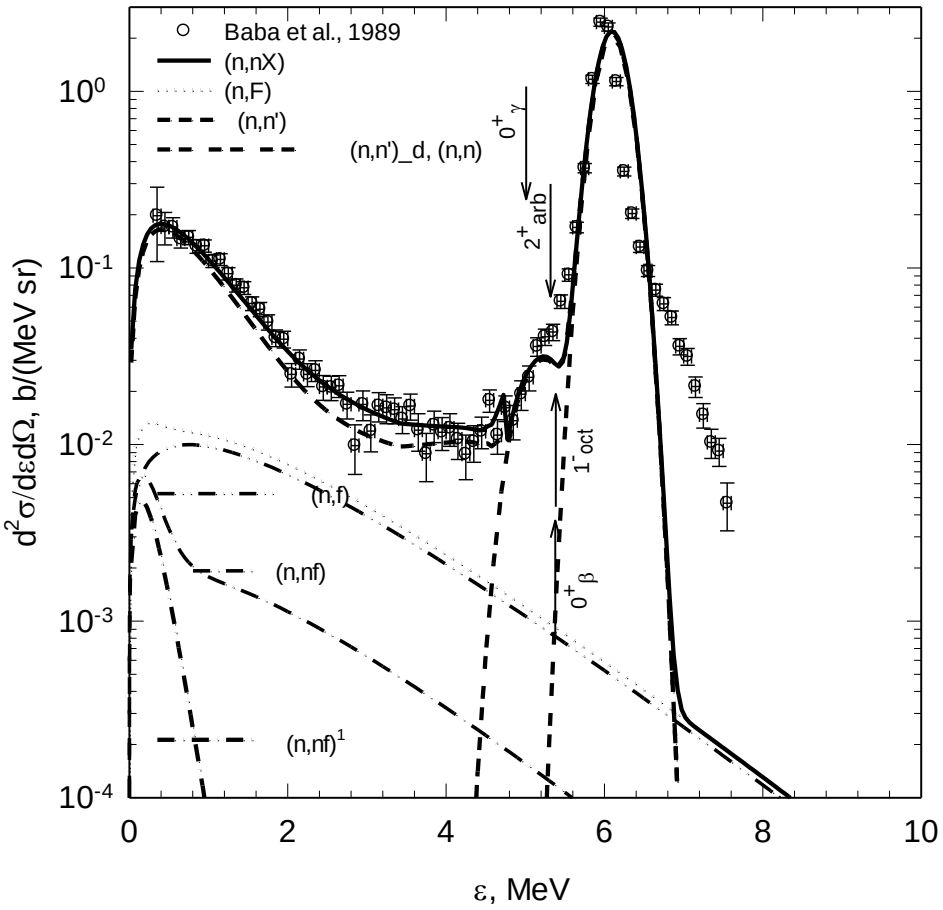

^{232}Th: E_n=6.1 MeV (120-deg.)

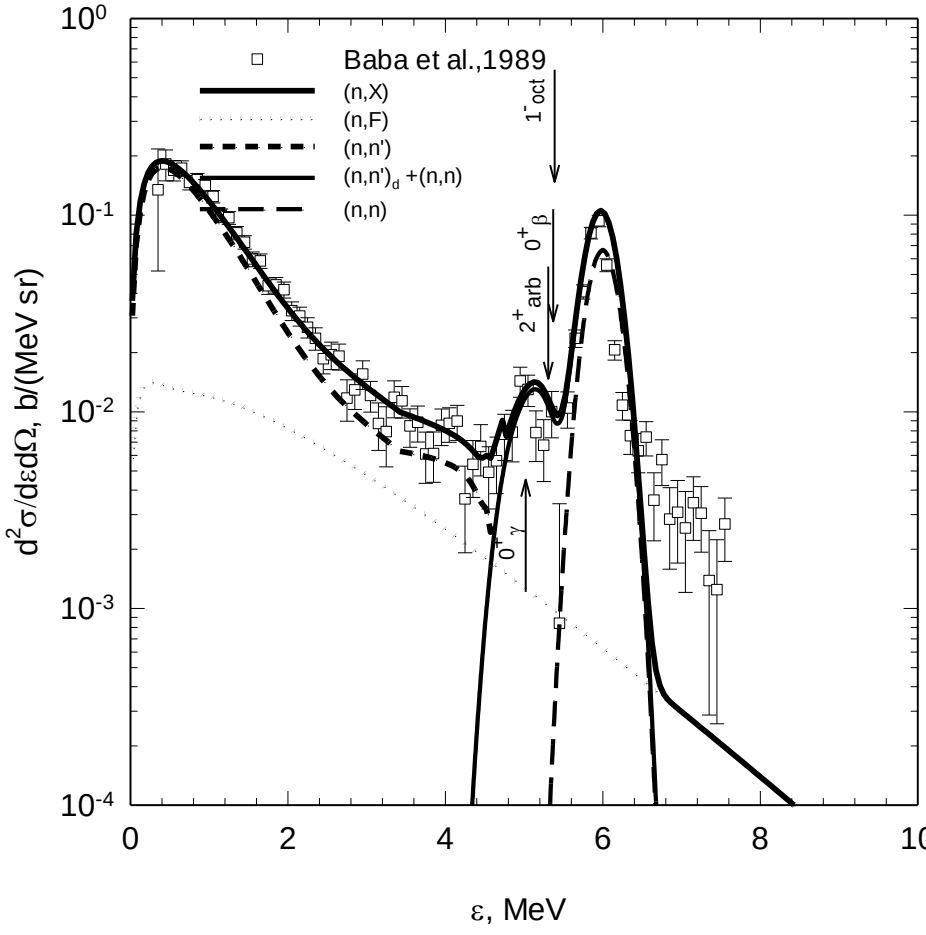

$$\frac{d^2\sigma(\varepsilon,E_n,\theta)}{d\varepsilon d\theta}=\frac{1}{2\pi}\Big[\nu_p(E_n,\theta)\sigma_{nF}(E_n,\theta)S(\varepsilon,E_n,\theta)+\sigma_{nn\gamma}(\varepsilon,E_n,\theta)\frac{d^2\sigma^1_{nn\gamma}(\varepsilon,E_n,\theta)}{d\varepsilon d\theta}+$$

$$\sigma_{n2n}(\varepsilon,E_n,\theta)\left(\frac{d^2\sigma^1_{n2n}(\varepsilon,E_n,\theta)}{d\varepsilon d\theta}+\frac{d^2\sigma^2_{n2n}(\varepsilon,E_n,\theta)}{d\varepsilon d\theta}\right)+$$

$$\sigma_{n3n}(\varepsilon,E_n,\theta)\left(\frac{d^2\sigma^1_{n3n}(\varepsilon,E_n,\theta)}{d\varepsilon d\theta}+\frac{d^2\sigma^2_{n3n}(\varepsilon,E_n,\theta)}{d\varepsilon d\theta}+\frac{d^2\sigma^3_{n3n}(\varepsilon,E_n,\theta)}{d\varepsilon d\theta}\right)+$$

$$\sum_q\ \frac{d\sigma_{nn\gamma}(\varepsilon,E_q,E_n,\theta)}{d\theta}G(\varepsilon,E_q,E_n,\Delta_\theta)\Big],$$

$$G(\varepsilon,E_q,E_n,\Delta_\theta)=\frac{2}{\Delta_\theta\sqrt{\pi}}\exp\left\{-\left[\frac{\varepsilon-\left(E_n-E_q\right)}{\Delta_\theta}\right]^2\right\}$$

$$S(\varepsilon, E_n, \theta) = \widetilde{S}_{A+1}(\varepsilon, E_n, \theta) + \widetilde{S}_{A}(\varepsilon, E_n, \theta) + \widetilde{S}_{A-1}(\varepsilon, E_n, \theta) + \widetilde{S}_{A-2}(\varepsilon, E_n, \theta) =$$

$$\nu_p^{-1}(E_n, \theta) \cdot \Big\{ \nu_{p1}(E_n) \cdot \beta_1(E_n, \theta) S_{A+1}(\varepsilon, E_n, \theta) + \nu_{p2}(E_n - \left\langle E_{nnf}(\theta) \right\rangle) \beta_2(E_n, \theta) S_A(\varepsilon, E_n, \theta) +$$

$$+ \beta_2(E_n, \theta) \frac{d^2\sigma^1_{nnf}(\varepsilon, E_n, \theta)}{d\varepsilon d\varepsilon} + \nu_{p3}(E_n - B_n^A - \left\langle E^1_{n2nf}(\theta) \right\rangle - \left\langle E^2_{n2nf}(\theta) \right\rangle) \beta_3(E_n, \theta) S_{A-1}(\varepsilon, E_n, \theta) + \beta_3(E_n, \theta) \cdot$$

$$\left[\frac{d^2\sigma^1_{n2nf}(\varepsilon, E_n, \theta)}{d\varepsilon d\theta} + \frac{d^2\sigma^2_{n2nf}(\varepsilon, E_n, \theta)}{d\varepsilon d\theta} \right] + \nu_{p4}(E_n - B_n^A - B_n^{A-1} - \left\langle E^1_{n3nf}(\theta) \right\rangle - \left\langle E^2_{n3nf}(\theta) \right\rangle - \left\langle E^3_{n3nf}(\theta) \right\rangle) \cdot$$

$$\beta_4(E_n, \theta) S_{A-2}(\varepsilon, E_n, \theta) + \beta_4(E_n, \theta) \left[\frac{d^2\sigma^1_{n3nf}(\varepsilon, E_n, \theta)}{d\varepsilon d\theta} + \frac{d^2\sigma^2_{n3nf}(\varepsilon, E_n, \theta)}{d\varepsilon d\theta} + \frac{d^2\sigma^3_{n2nf}(\varepsilon, E_n, \theta)}{d\varepsilon d\theta} \right] \Big\}.$$

$$U_x = E_n + B_n - \sum_{x,1\le k\le x}(< E^k_{nxnf}(\theta) > + B_{nx})$$

$$E_{nx} = E_r - E^{pre}_{fx} + E_n + B_n - \sum_{x,1\le k\le x}\left(\left\langle E^k_{nxnf}(\theta)\right\rangle + B_{nx}\right)$$

$$E^{post}_F \approx E^{pre}_F\left(1-\nu_{post}/\left(A+1-\nu_{pre}\right)\right)$$

$$\nu_{\mathrm{p}}(E_n) = \nu_{post} + \nu_{pre} = \sum_{x=1}^{X}\nu_{px}(E_{nx}) + \sum_{x=1}^{X}(x-1)\cdot\beta_x(E_n)$$

$$\sigma_{nF}(E_n) = \sigma_{nf}(E_n) + \sum_{x=1}^{X} \sigma_{n,xnf}(E_n)$$

$$\sigma_{n,xnf}(E_n) = \sum_{J\pi} \int_0^{U_x} W_{A+1-x}^{J\pi}(U) P_{f(A+1-x)}^{J\pi}(U) dU$$

$$\frac{d^2\sigma_{nnx}^1(\varepsilon, E_n, \theta)}{d\varepsilon d\theta} \approx \frac{d^2\tilde{\sigma}_{nnx}^1(\varepsilon, E_n, \theta)}{d\varepsilon d\theta} + \sqrt{\frac{\varepsilon}{E_n}} \frac{\omega(\theta)}{E_n - \varepsilon}$$

$$\omega(\theta) = 0.4\cos^3(\theta) + 0.16$$

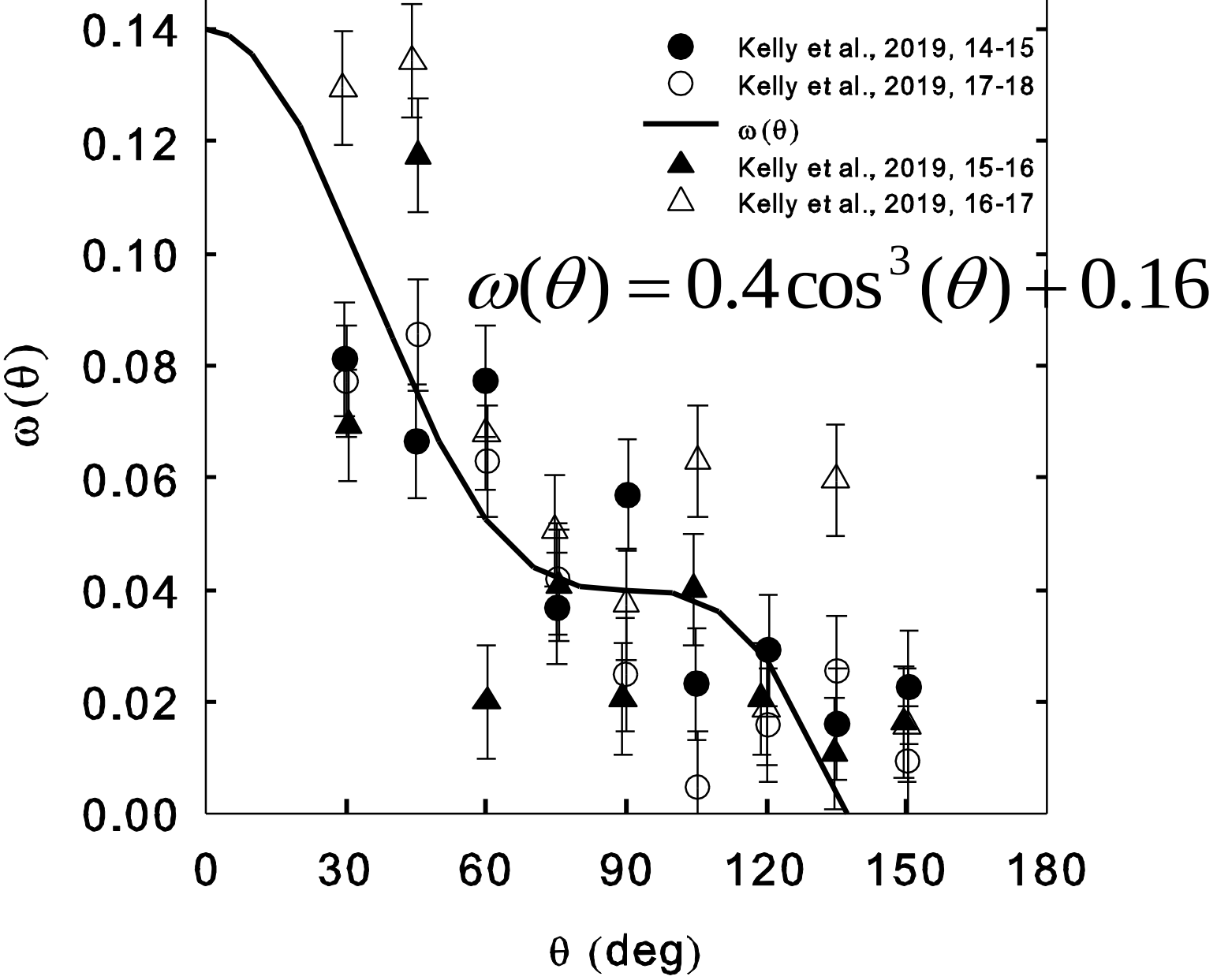
Kelly et al., 2019, 14-15
Kelly et al., 2019, 17-18
ω(θ)
Kelly et al., 2019, 15-16
Kelly et al., 2019, 16-17
$\omega(\theta) = 0.4\cos^3(\theta) + 0.16$
ω(θ)
0.14
0.12
0.10
0.08
0.06
0.04
0.02
0.00
0
30
60
90
120
150
180
θ (deg)

$$\frac{d\sigma^{1}_{nnx}(\varepsilon, E_n)}{d\varepsilon} \approx \frac{d\tilde{\sigma}^{1}_{nnx}(\varepsilon, E_n)}{d\varepsilon} + \sqrt{\frac{\varepsilon}{E_n}} \frac{\langle \omega(\theta) \rangle_\theta}{E_n - \varepsilon}$$

$$\sigma_c(E_n) = \sigma_a(E_n)\left(1 - q - \tilde{q}\right),$$

$$\tilde{q} = \int_0^{E_n - E_d} \frac{d\tilde{\sigma}^{1}_{nnx}}{d\varepsilon} d\varepsilon = \int_0^{E_n - E_d} \sqrt{\frac{\varepsilon}{E_n}} \frac{\langle \omega(\theta) \rangle_\theta}{E_n - \varepsilon} d\varepsilon = \langle \omega(\theta) \rangle_\theta \left[\ln\left(\frac{1 + \sqrt{1-\delta}}{1 - \sqrt{1-\delta}} \right) - 2\sqrt{1-\delta} \right]$$

$\delta = E_d / E_n$

$$\frac{d\tilde{\sigma}^1_{nnx}(\varepsilon, E_n)}{d\varepsilon} = \sum_{J,\pi} W^A(E_n - \varepsilon, \theta, J^\pi)$$

$$\frac{d^2\sigma^1_{nnf}(\varepsilon, E_n, \theta)}{d\varepsilon d\theta} = \frac{d^2\sigma^1_{nnx}(\varepsilon, E_n, \theta)}{d\varepsilon d\theta} \frac{\Gamma^A_f(E_n - \varepsilon, \theta)}{\Gamma^A(E_n - \varepsilon, \theta)}.$$

$$\frac{d^2\sigma^1_{n2nx}(\varepsilon, E_n, \theta)}{d\varepsilon d\theta} = \frac{d^2\sigma^1_{nnx}(\varepsilon, E_n, \theta)}{d\varepsilon d\theta} \frac{\Gamma^A_n(E_n - \varepsilon, \theta)}{\Gamma^A(E_n - \varepsilon, \theta)}$$

$$\frac{d^2\sigma^1_{n2nf}(\varepsilon, E_n, \theta)}{d\varepsilon d\theta} = \int_0^{E - B^A_n} \frac{d^2\sigma^1_{n2nx}(\varepsilon, E_n, \theta)}{d\varepsilon d\theta} \frac{\Gamma^{A-1}_f(E_n - B^A_n - \varepsilon - \varepsilon_1)}{\Gamma^{A-1}(E_n - B^A_n - \varepsilon - \varepsilon_1)} d\varepsilon_1$$

232Th NES 6.1 MeV 30 deg

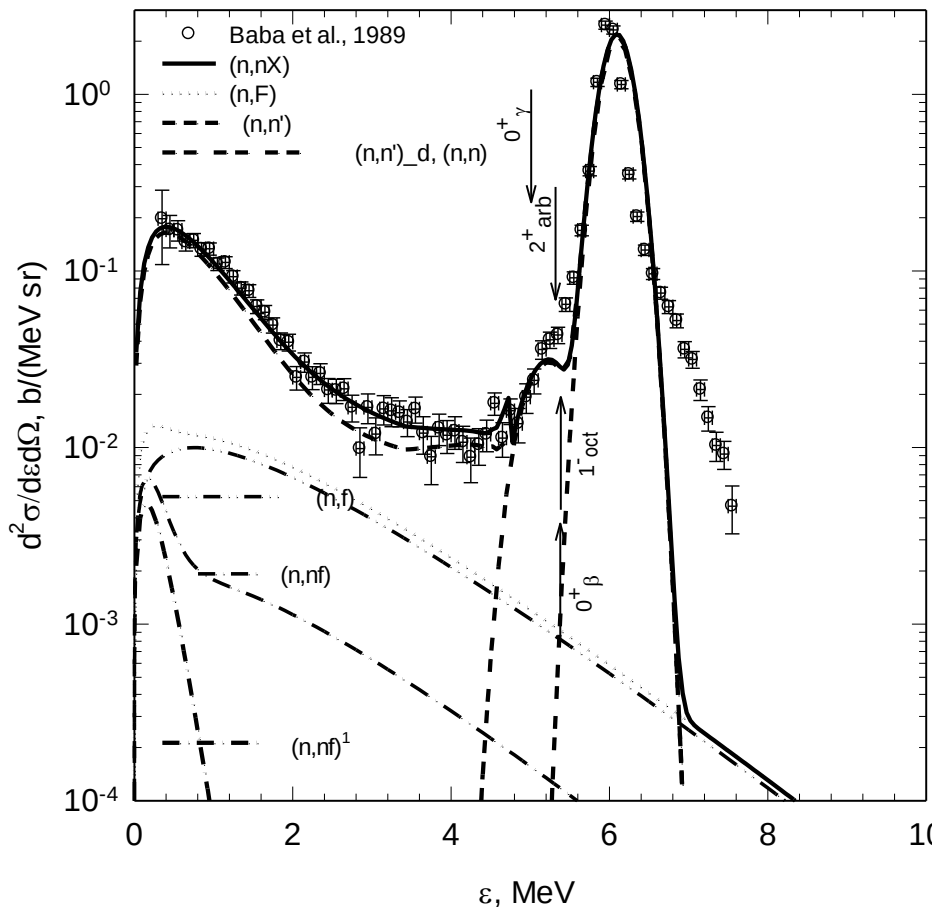

^{232}Th: E_n=6.1 MeV (45-deg.)

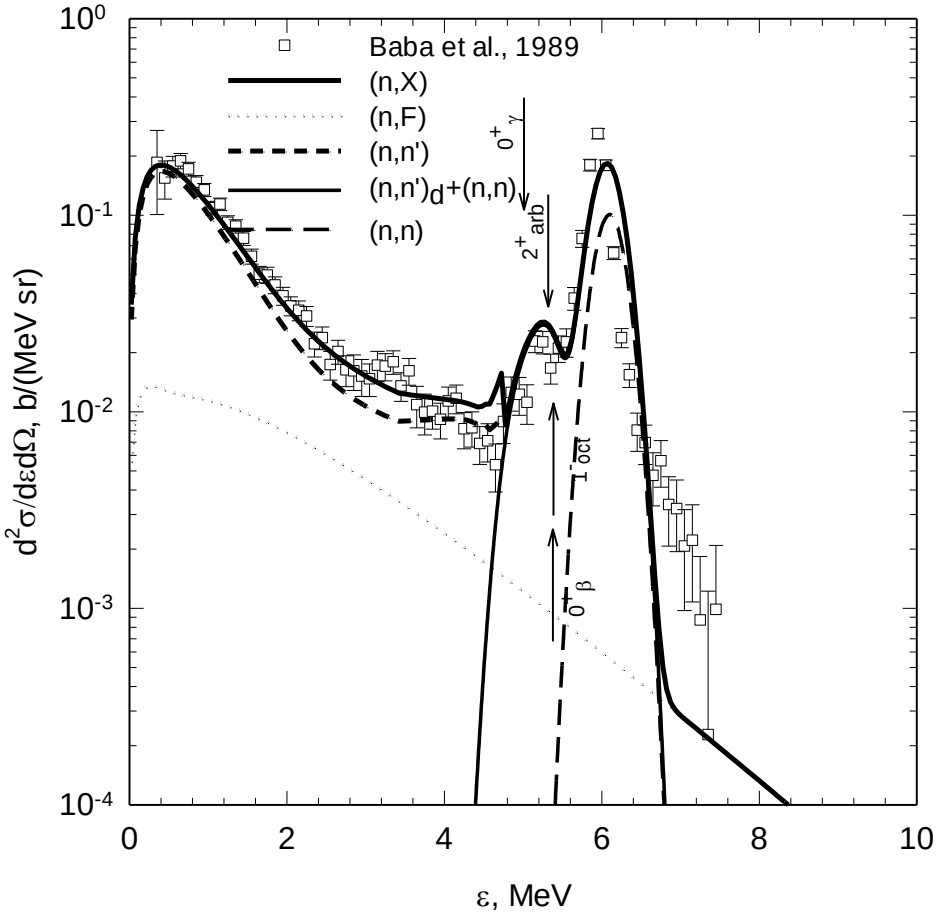

^{232}Th: E_n=6.1 MeV (60-deg.)

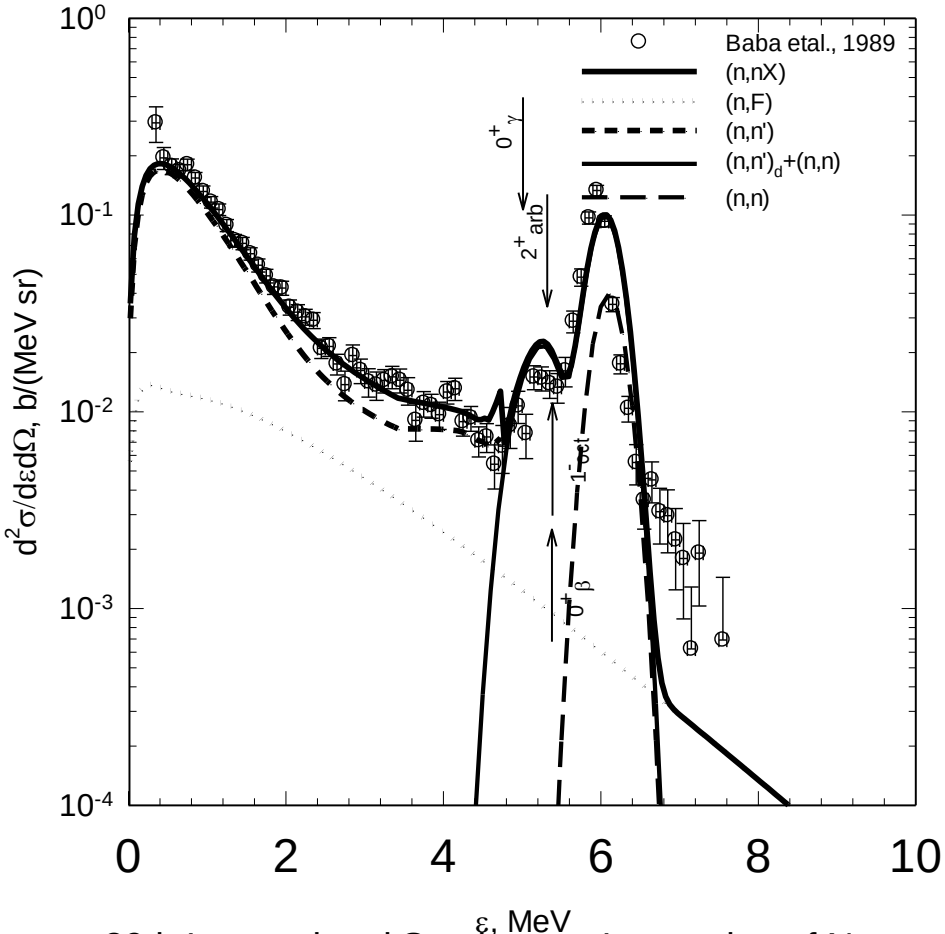

^{232}Th: E_n=6.1 MeV (90-deg.)

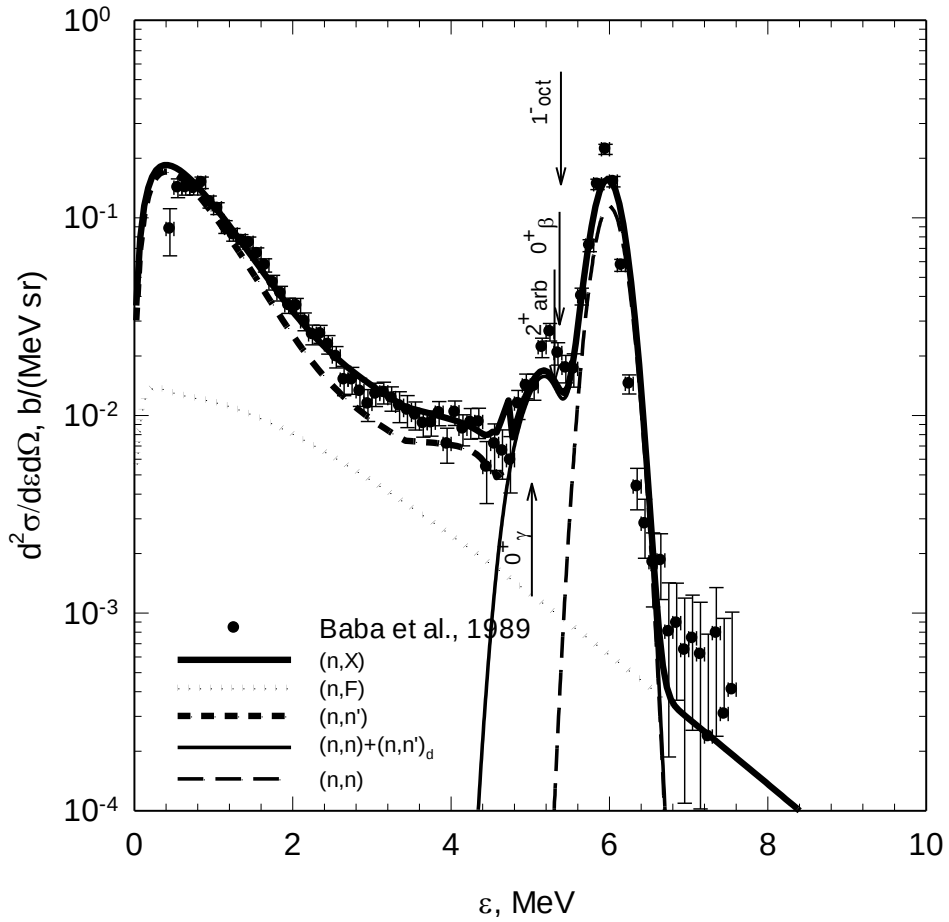

232Th NES 11.8 MeV 30 deg

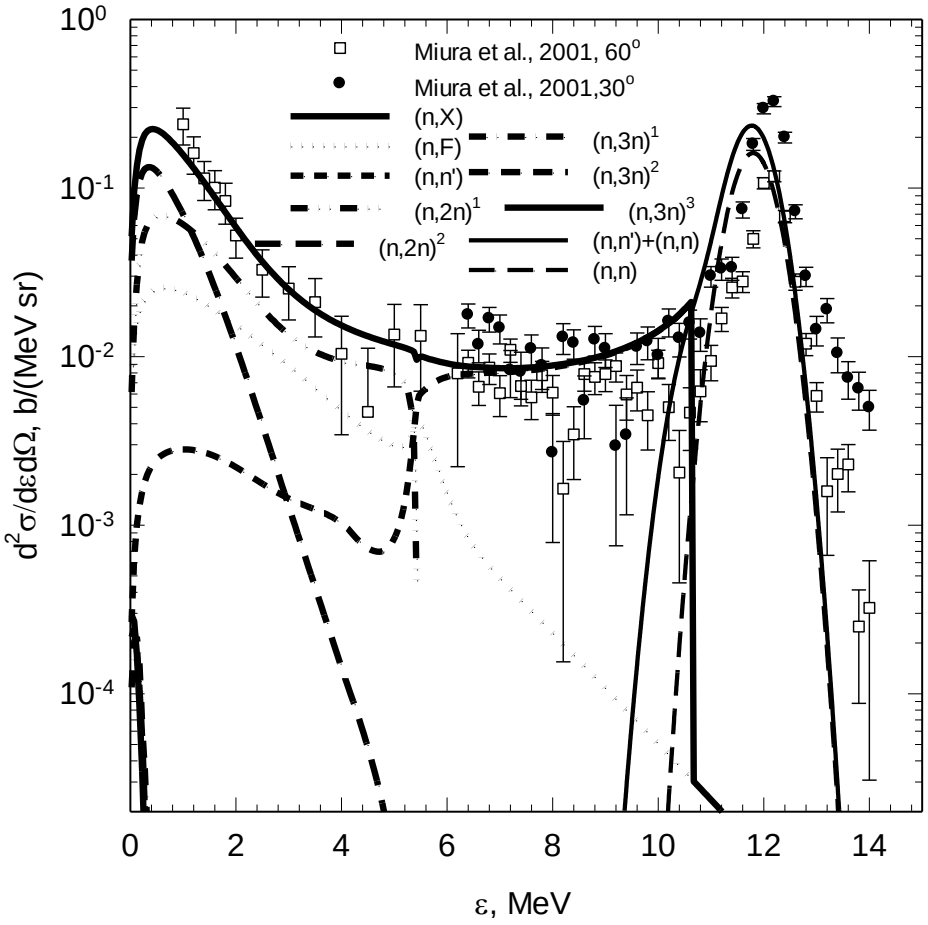

232Th NES 11.8 MeV 90 deg

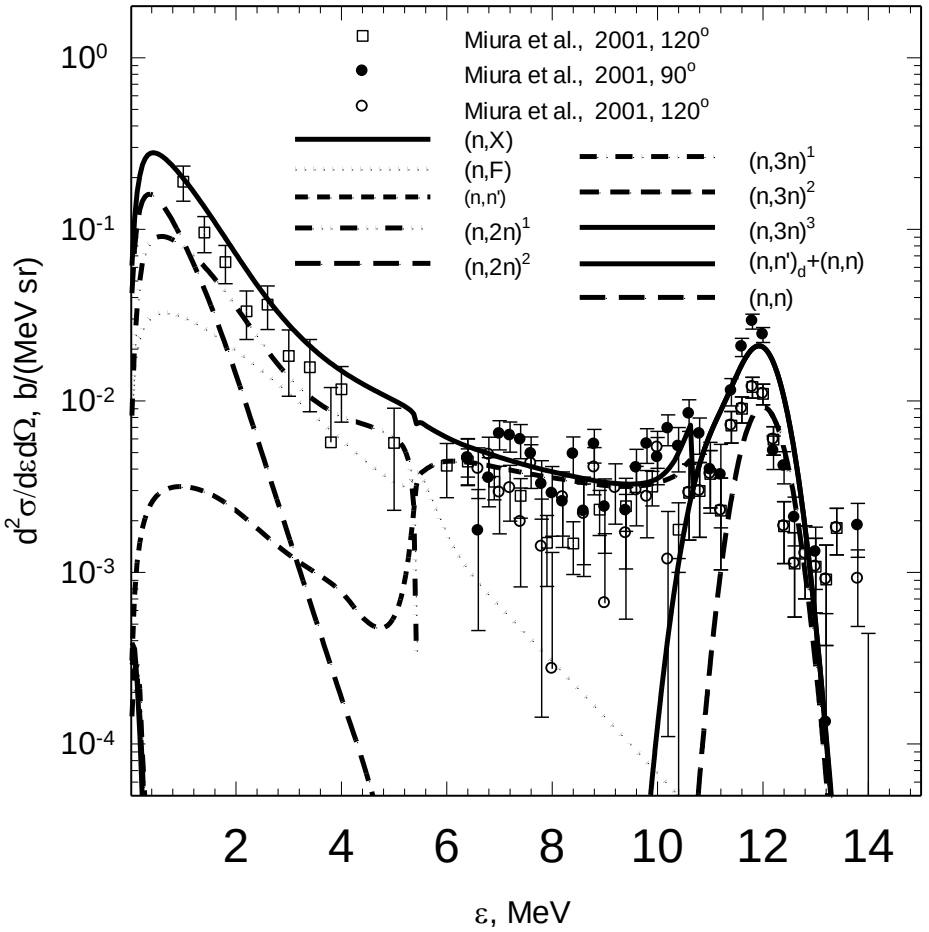

232Th NES 11.8 MeV 30 deg

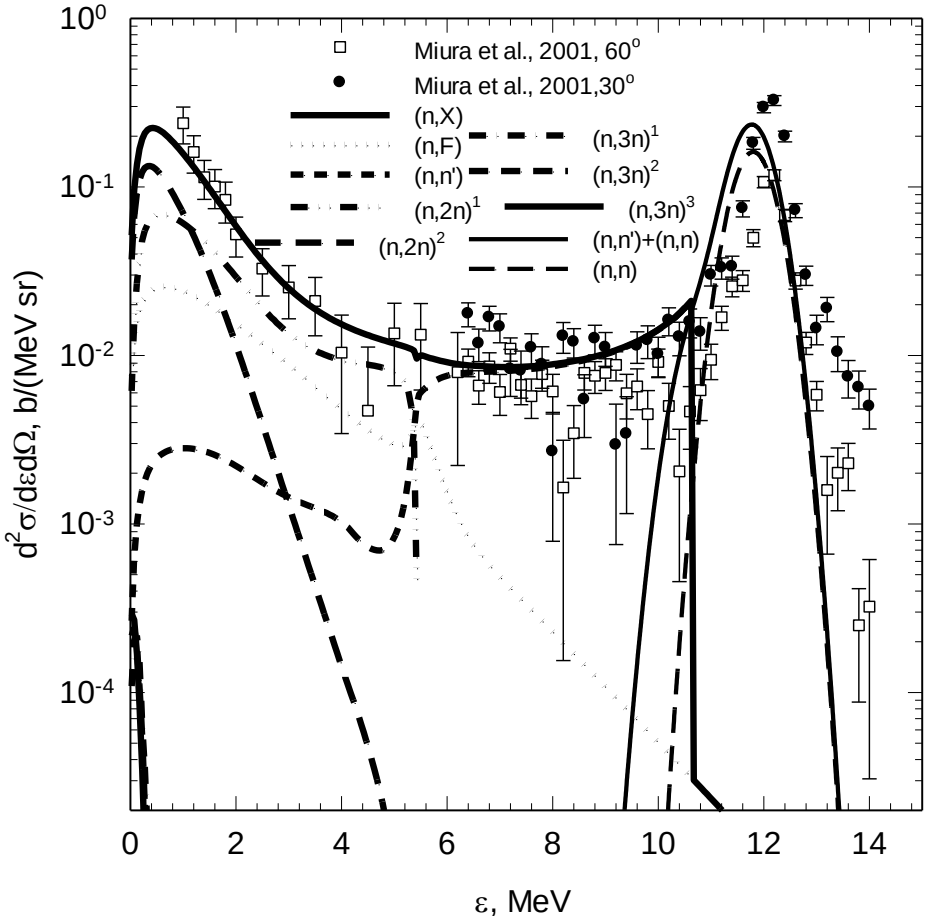

232Th NES 11.8 MeV 120 deg

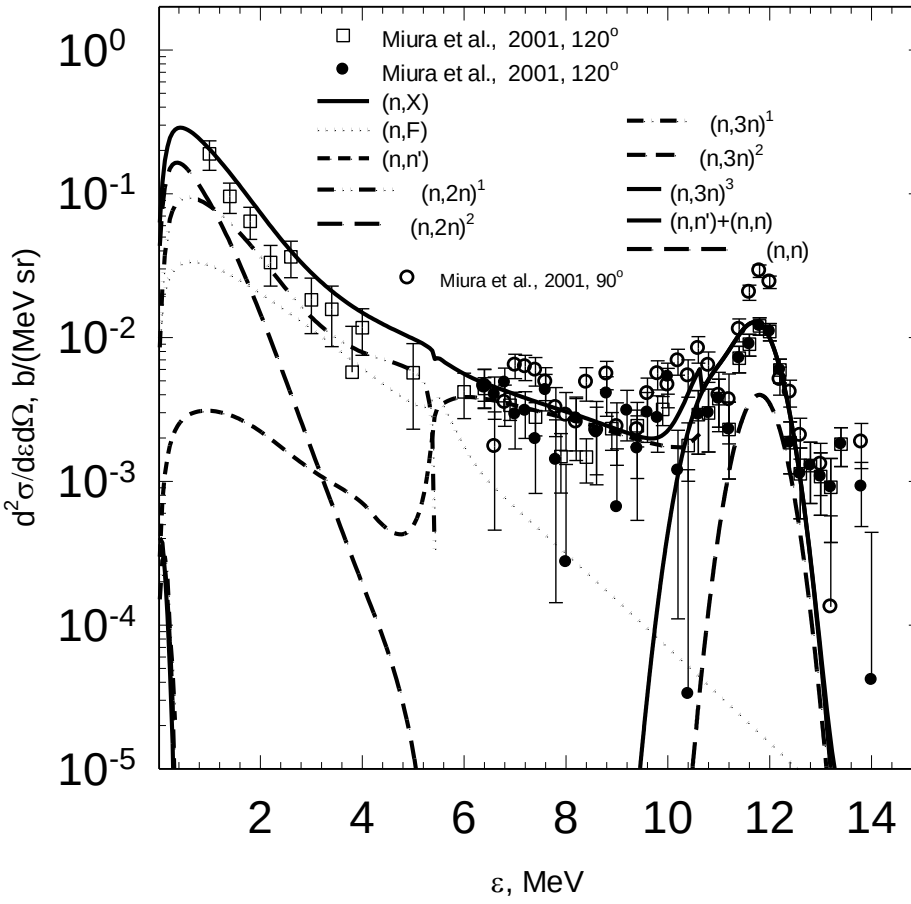

232Th NES 14 MeV 30 deg.

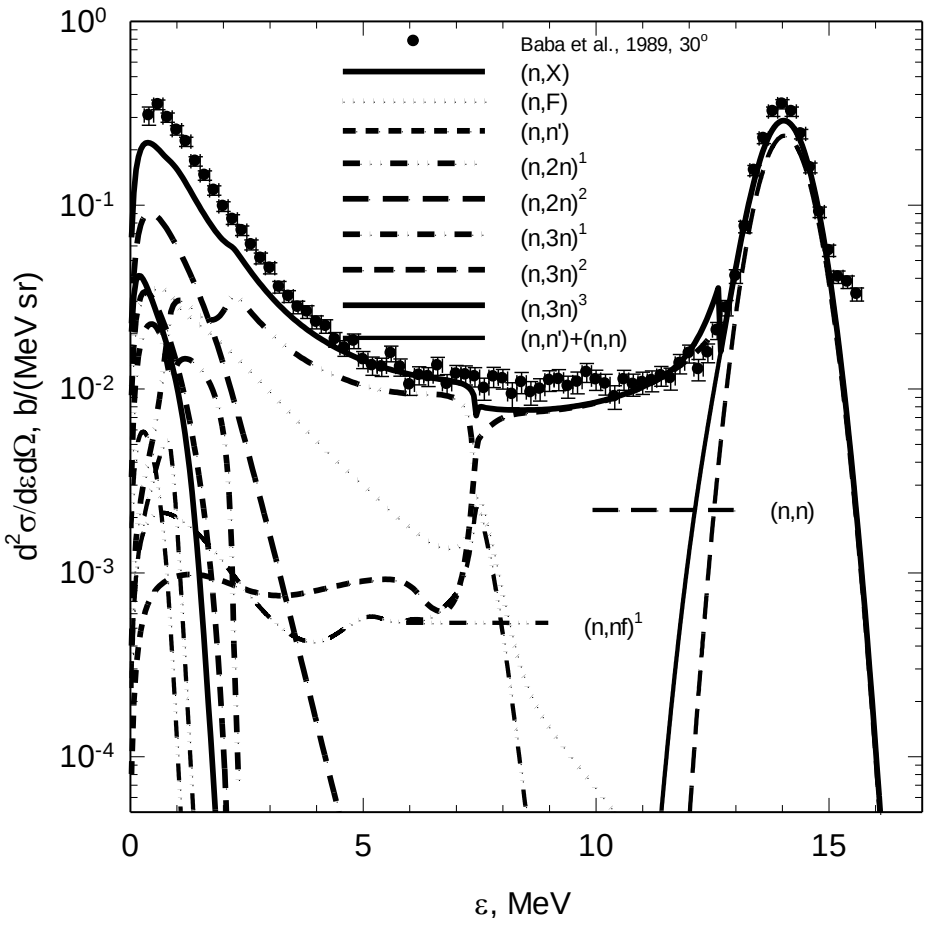

232Th NES14 MeV 120 deg

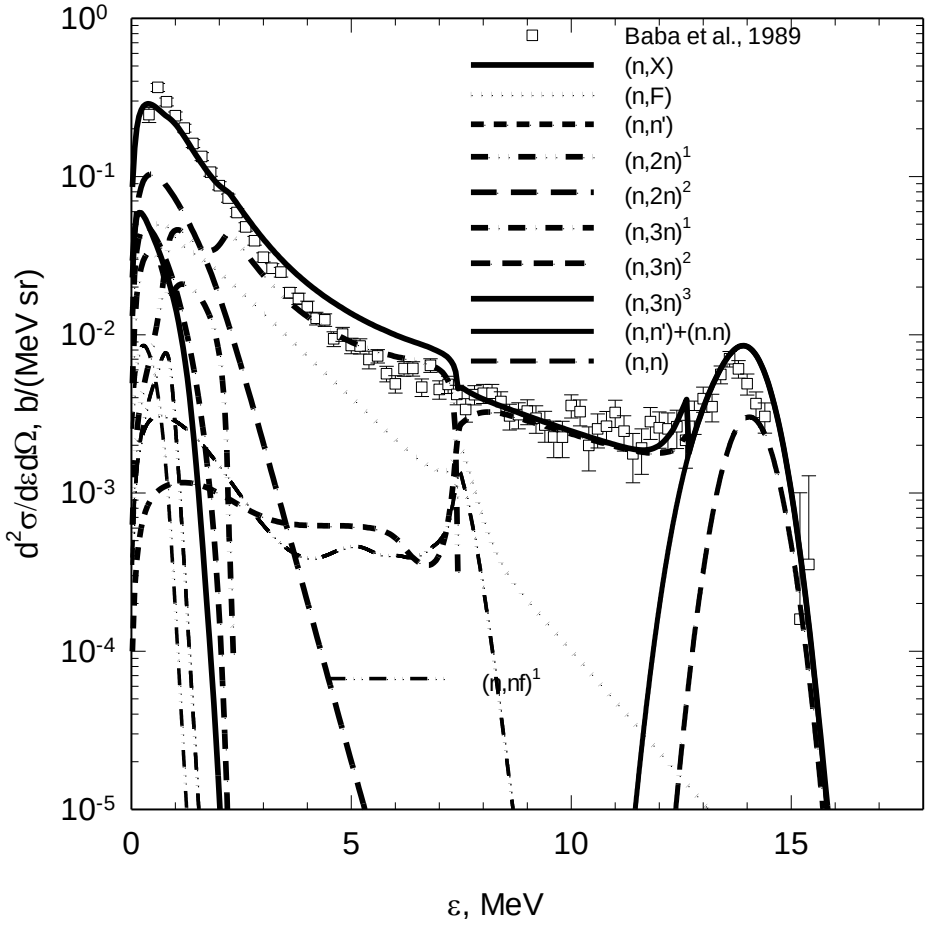

232Th NES14 MeV 30 deg

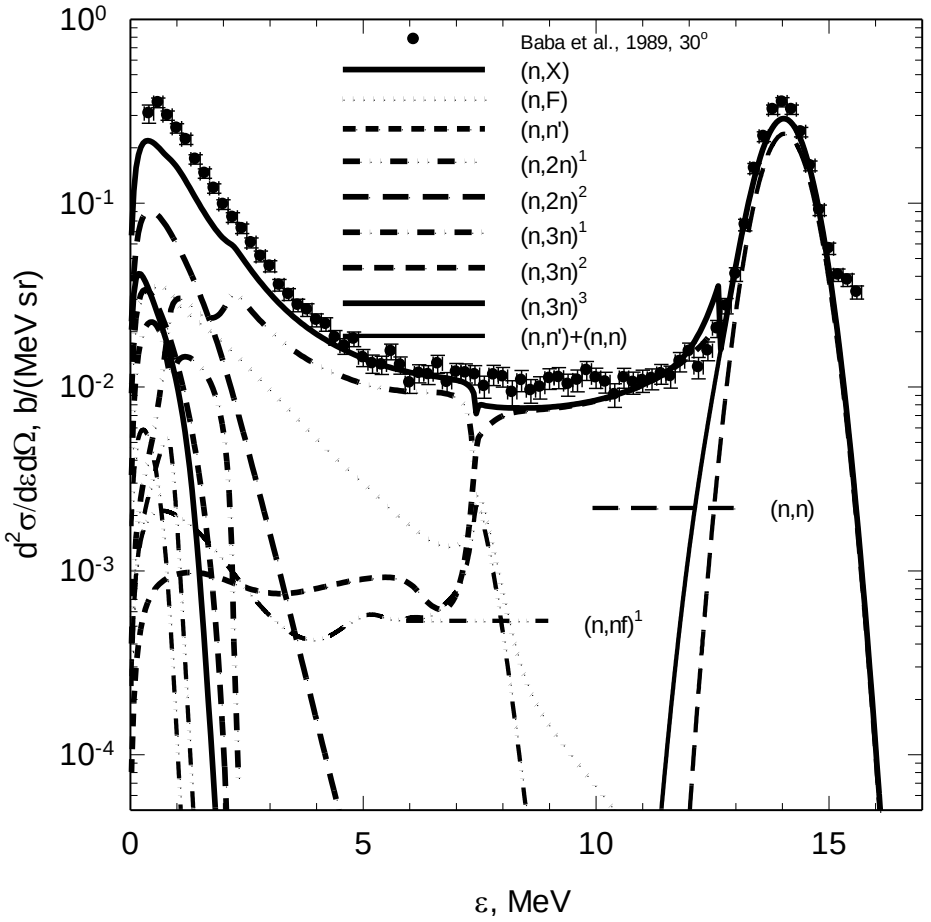

232Th NES14 MeV 90 deg

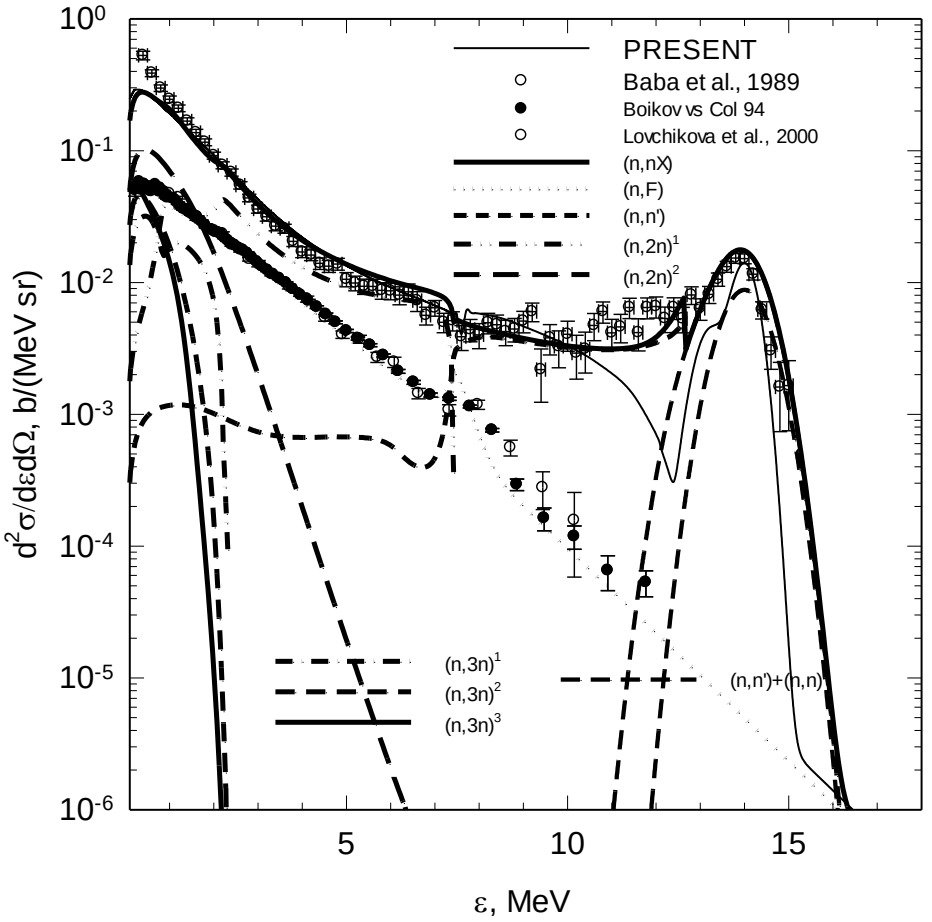

232Th NES, 18 MeV 30 deg

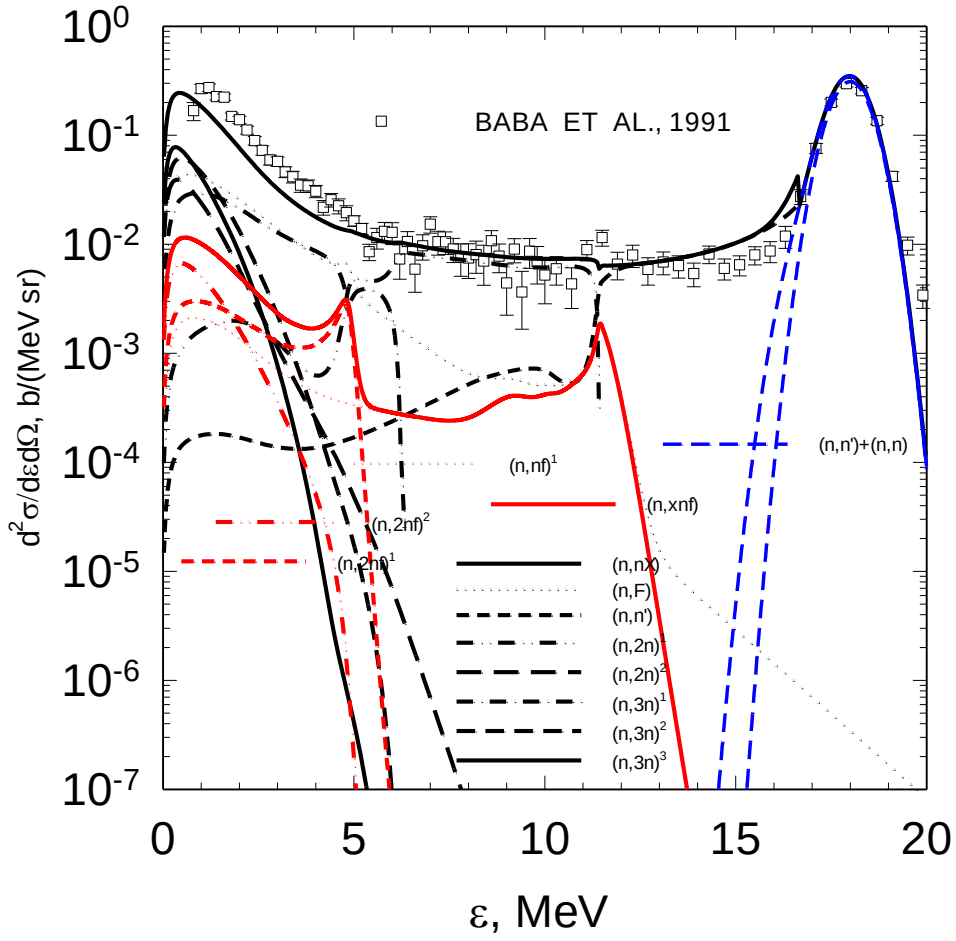

232Th NES18 MeV 120 deg

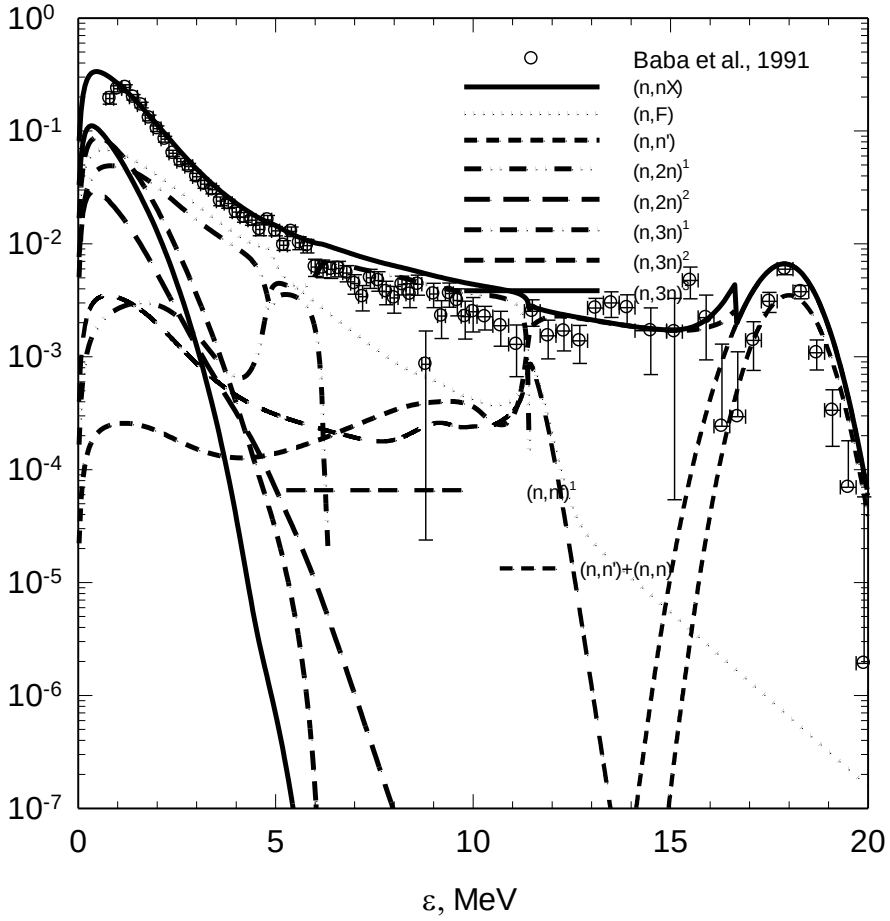

232Th(n,F) 17.7 MeV

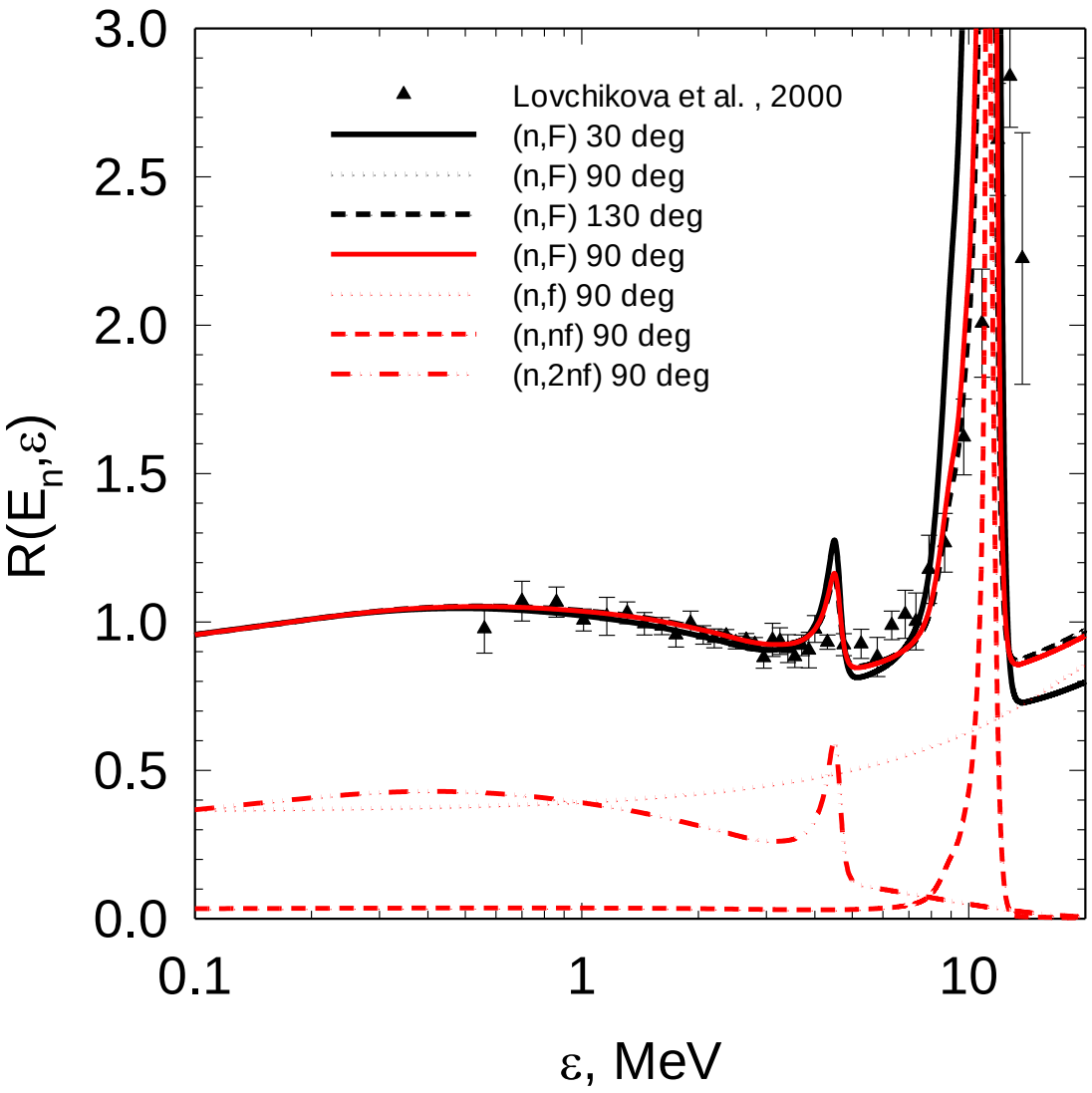

^{232}Th FISSION CROSS SECTION

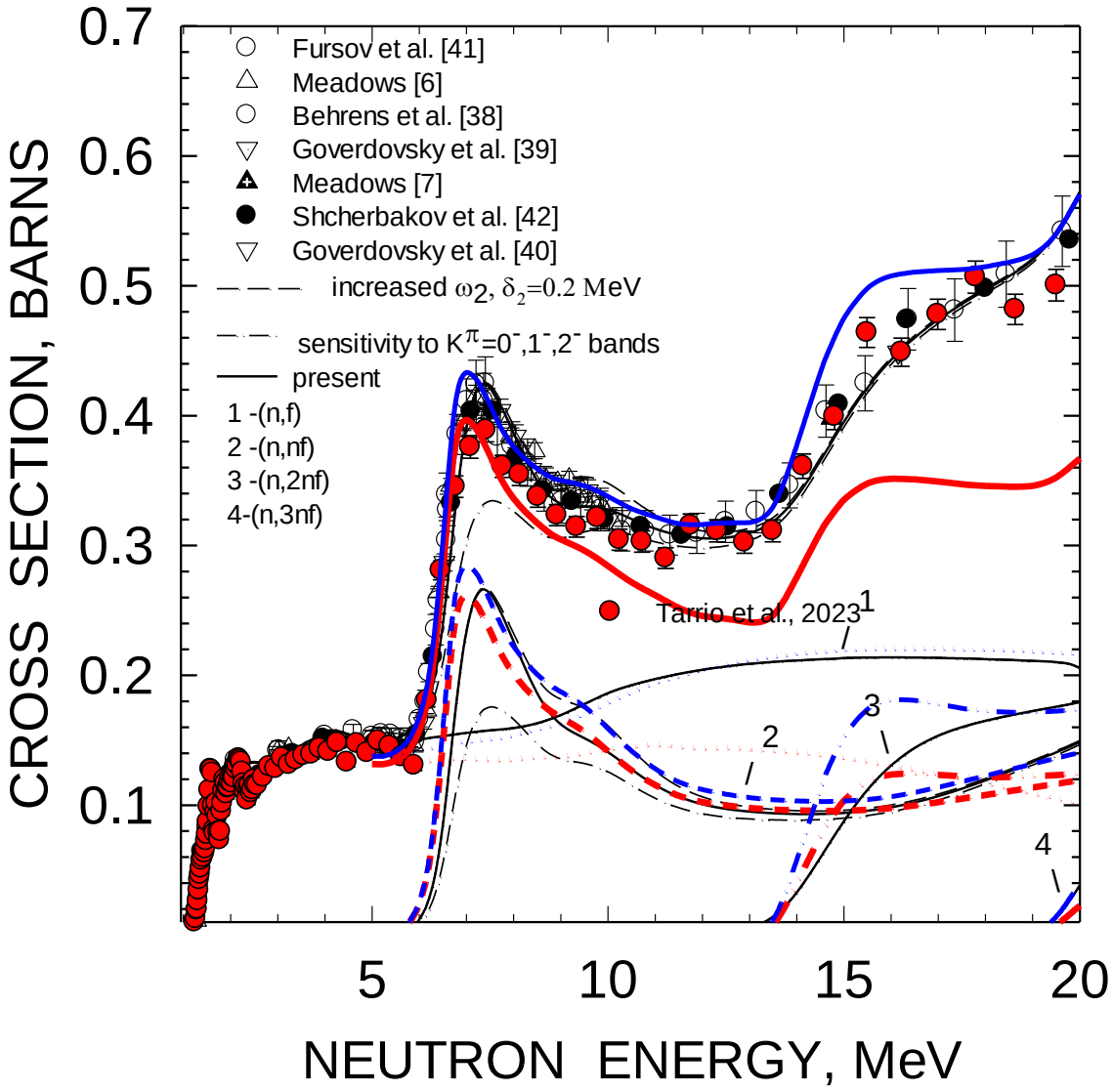

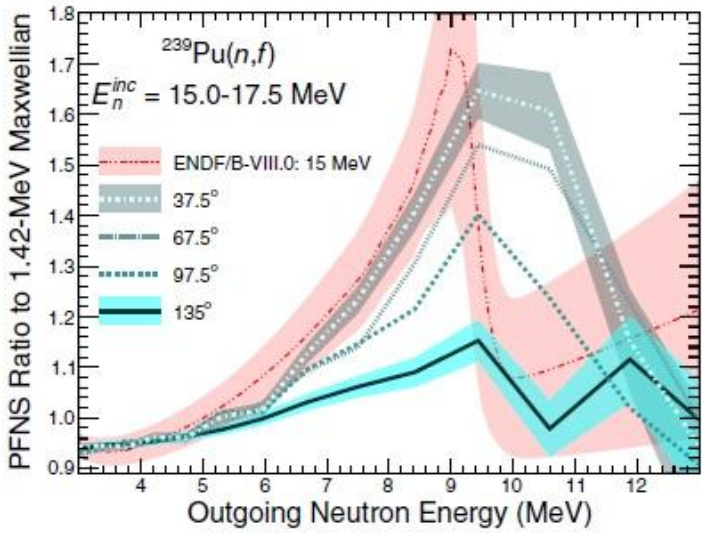

FIG. 3. The angular dependence of the fission neutron spectrum of $^{239}\mathrm{Pu}(n,f)$ is shown. Lines of different styles and shades of blue correspond to different detection angles. The width of the largest and smallest angles represents the statistical uncertainty. The uncertainties for the intermediate angles are not shown but are similar. The ENDF/B-VIII.0 [3] PFNS at $E_n^{\mathrm{inc}} = 15$ MeV is shown as the red dash-triple-dotted line and shaded region, the latter of which represents the evaluation uncertainty. Note that the preequilibrium neutrons are clearly observed even at angles above 90°. All spectra were scaled to have the same integral in the 3–5 MeV outgoing neutron energy range.

the peak of the excess appears to be shifted downward with respect to the incident neutron energy by approximately the fission binding energy (≈6 MeV), as expected for prefission preequilibrium neutron spectra [4]. Figure 3 shows the behavior of the excess observed for an incident energy range of $E_n^{\mathrm{inc}} = 15.0$–$17.5$ MeV as a function of detection angle compared to the ENDF/B-VIII.0 [3] evaluated PFNS for $E_n^{\mathrm{inc}} = 15$ MeV. Note that the ENDF/B-VIII.0 spectra are not differentiated by angle and are assumed to be integrated over all observable angles. The onset energy of this PFNS feature appears consistent with the ENDF/B-VIII.0 prediction, further suggesting that this feature is the preequilibrium prefission component of the PFNS. Additionally, Fig. 3 demonstrates the observation of the expected forward-peaked angular distribution with respect to the momentum direction of the incident neutron beam, which is not to be confused with the orientation of the fission axis.

The strongly anisotropic character of the preequilibrium prefission neutrons implies that the observed PFNS should be harder (i.e., higher average PFNS energy) at forward (small) angles than it is at backward (large) angles once preequilibrium neutron emission is present. This effect is shown in Fig. 4 through the ratio of the average PFNS energy at the minimum detection angle to that of the maximum detection angle for an outgoing PFNS energy

$$\frac{\sigma_{n,2nf}(E_n,\theta)}{4\pi}\frac{d\sigma^{1,2}_{n2nf}(\varepsilon,E_n,\theta)}{d\varepsilon}$$

$$R(\varepsilon,15\div17.5)\approx\frac{\int_{15}^{17.5}\nu_p(E_n,\approx30^o)\sigma_{nF}(E_n,\approx30^o)S(\varepsilon,E_n,\theta\approx30^o)\varphi(E_n)dE_n}{\int_{15}^{17.5}\nu_p(E_n,\theta\approx135^o)\sigma_{nF}(E_n,\theta\approx135^o)S(\varepsilon,E_n,\theta\approx135^o)\varphi(E_n)dE_n}$$

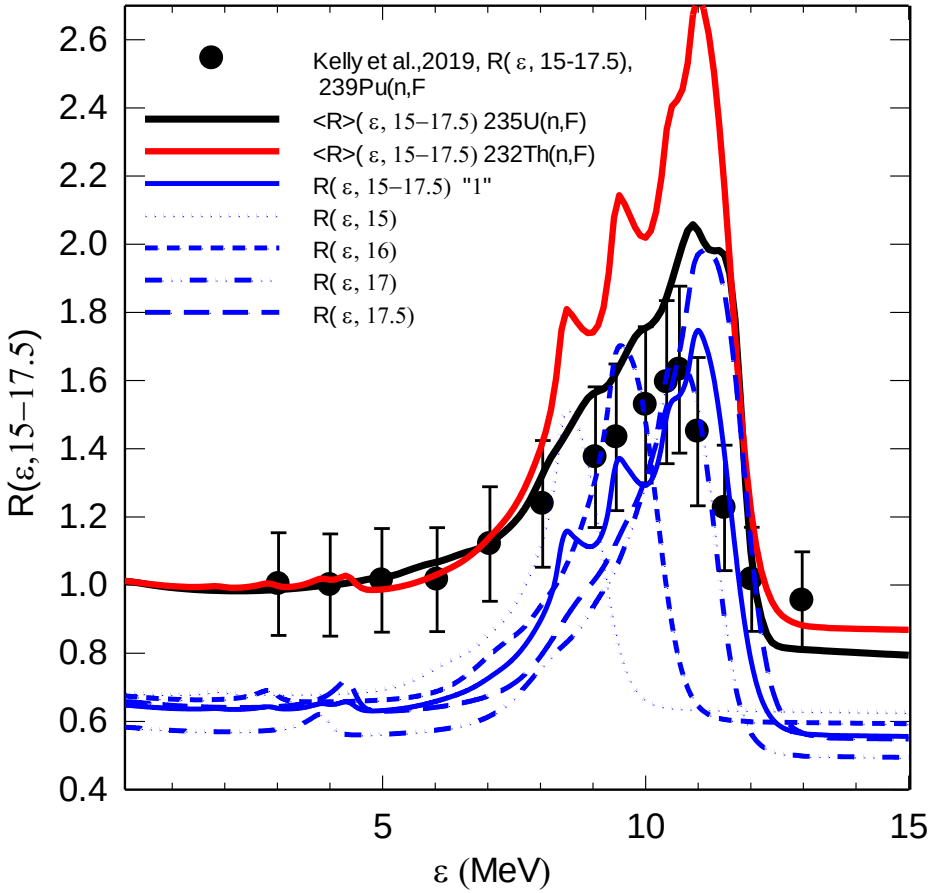
Kelly et al.,2019, R(ε, 15-17.5), 239Pu(n,F
<R>(ε, 15–17.5) 235U(n,F)
<R>(ε, 15–17.5) 232Th(n,F)
R(ε, 15–17.5) "1"
R(ε, 15)
R(ε, 16)
R(ε, 17)
R(ε, 17.5)
R(ε,15–17.5)
ε (MeV)
2.6
2.4
2.2
2.0
1.8
1.6
1.4
1.2
1.0
0.8
0.6
0.4
5
10
15

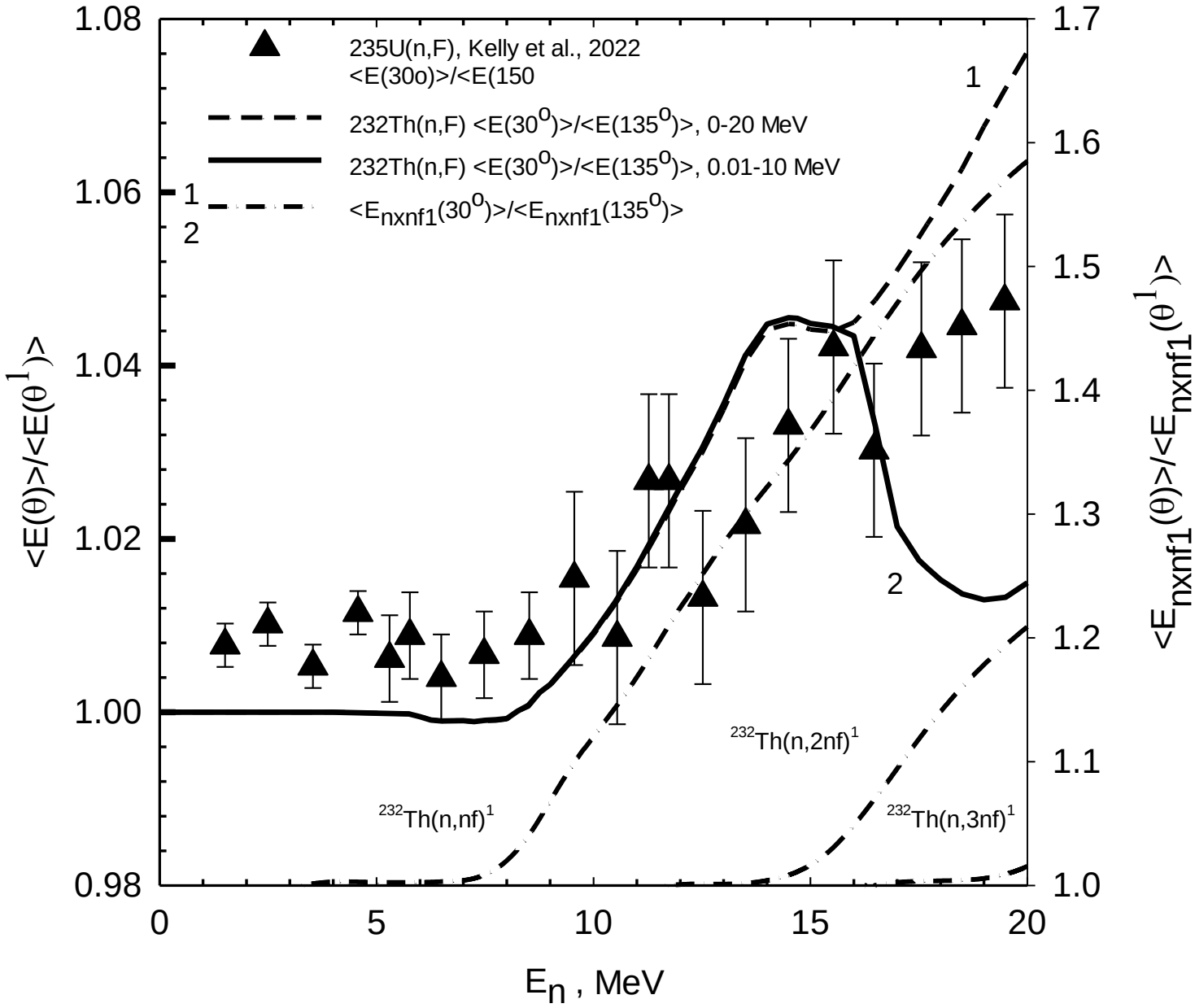
235U(n,F), Kelly et al., 2022
<E(30o)>/<E(150
232Th(n,F) <E(30^O)>/<E(135^O)>, 0-20 MeV
232Th(n,F) <E(30^O)>/<E(135^O)>, 0.01-10 MeV
<E_nxnf1(30^O)>/<E_nxnf1(135^O)>
1
2
<E(θ)>/<E(θ^1)>
<E_nxnf1(θ)>/<E_nxnf1(θ^1)>
232Th(n,nf)^1
232Th(n,2nf)^1
232Th(n,3nf)^1
E_n , MeV

Exclusive neutron spectra of $(n,xnf)^{1,..x}$, $(n,n\gamma)$ and $(n,xn)^{1,..x}$ are calculated within Hauser-Feshbach formalism alongside with (n,F) and (n,xn) reaction cross sections,
angular dependence of first $(n,nX)^1$ emission $W(\theta)$ being included.

235U(n,F) PFNS 6 MeV

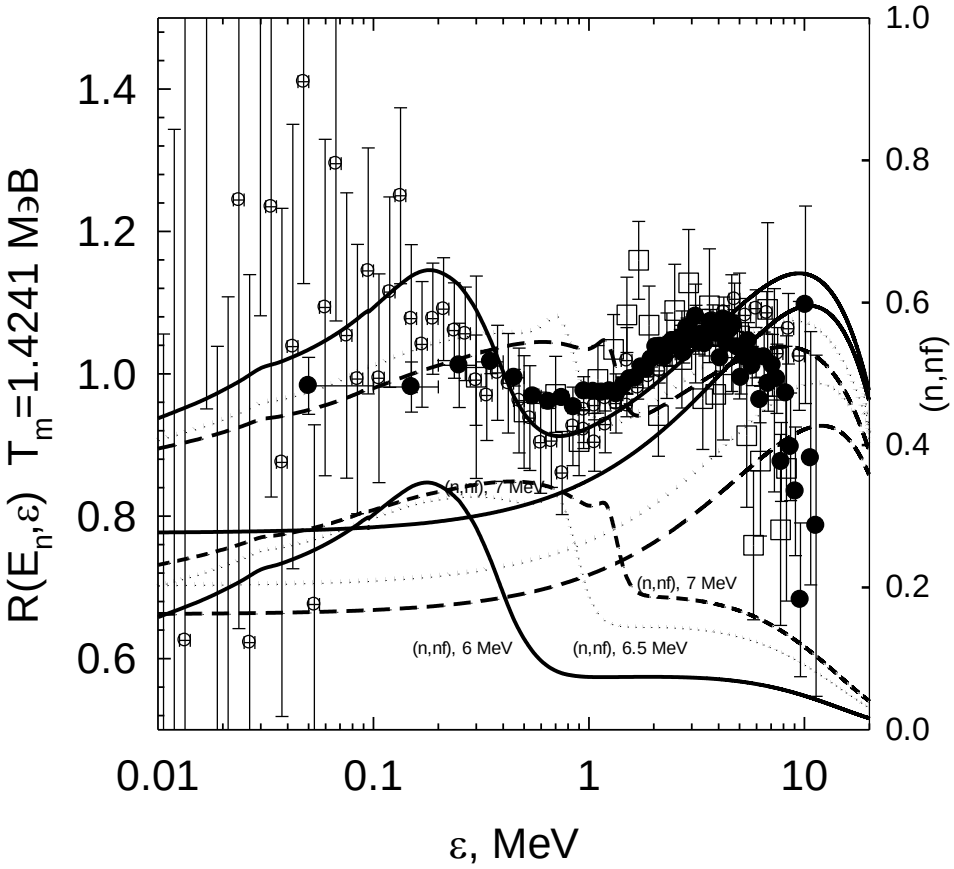

235U (n,F) PFNS 6.5 MeV

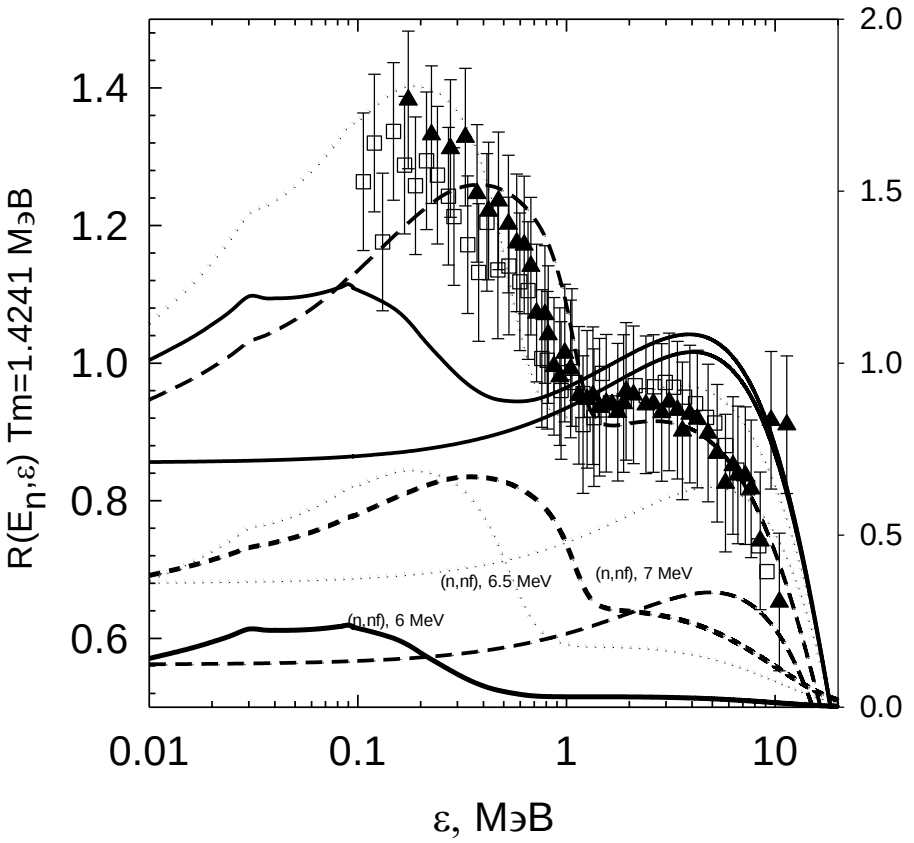

V.M. Maslov, N.V. Kornilov, A.B. Kagalenko and N.A. Tetereva, Nucl. Phys. A**760**, 274 (2005); https://www.sciencedirect.com/science/article/abs/pii/S037594740500933 4; https://www-nds.iaea.org/minskact/data/92235f18.txt.

235U(n,F) 6,6.5 7 MeV

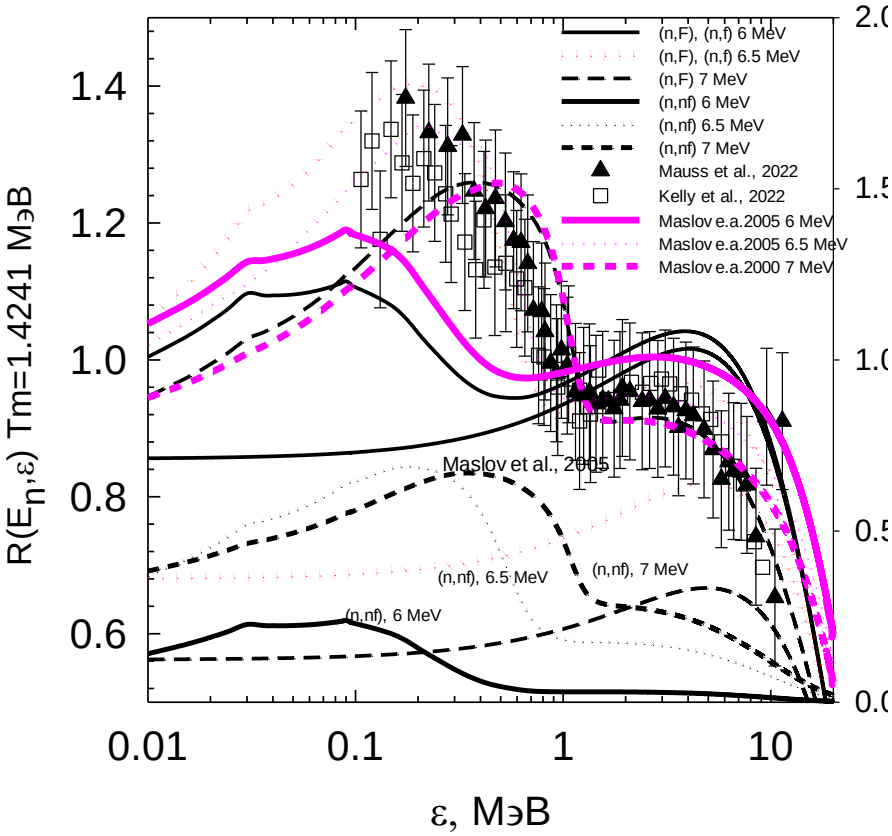

235U(n,F) CENDL-3.2 5, 6, 7 MeV

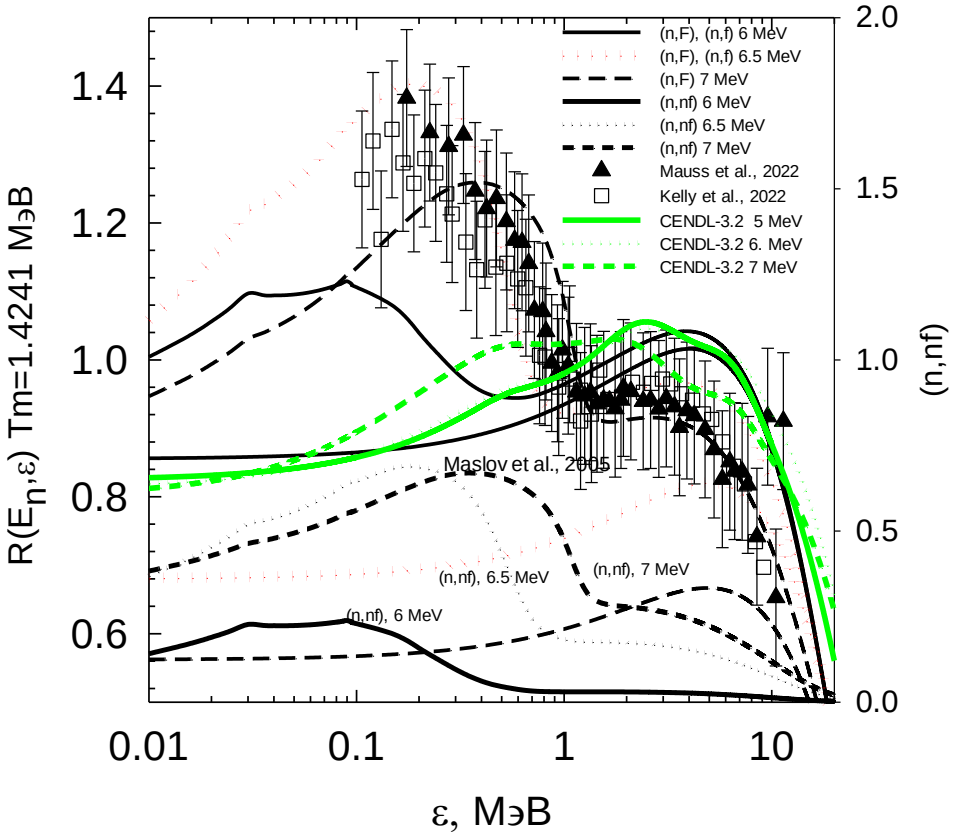

235U(n,F) JEFF-3.3 6,6.5 7 MeV

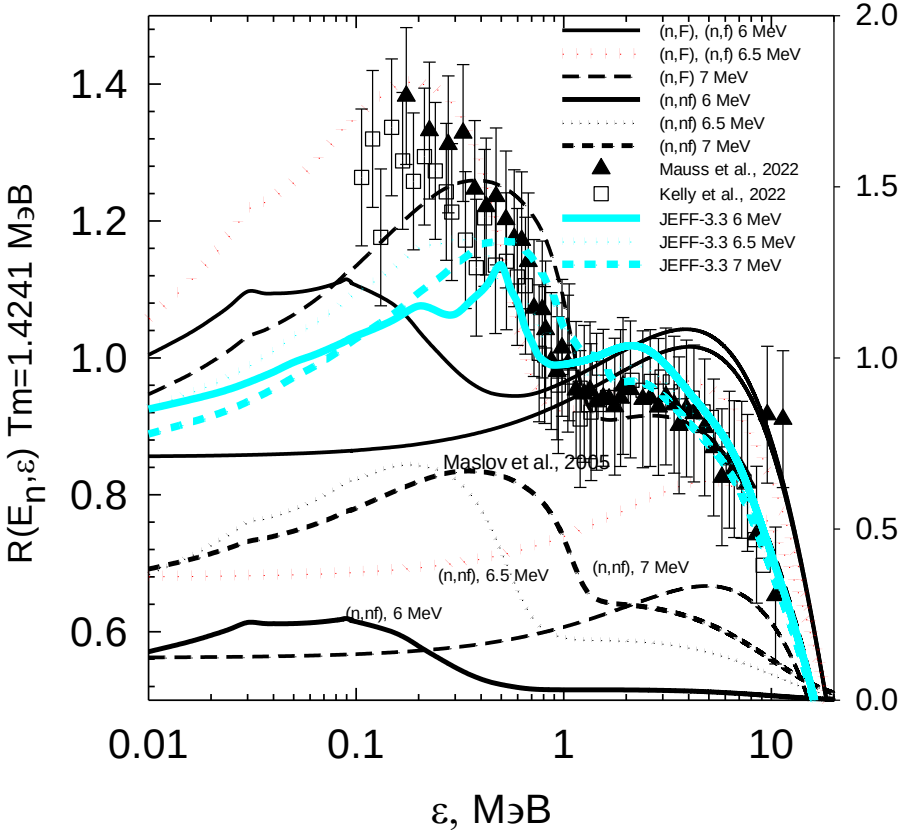

235U(n,F) ENDF/B-VIII 6, 6.5 7 MeV

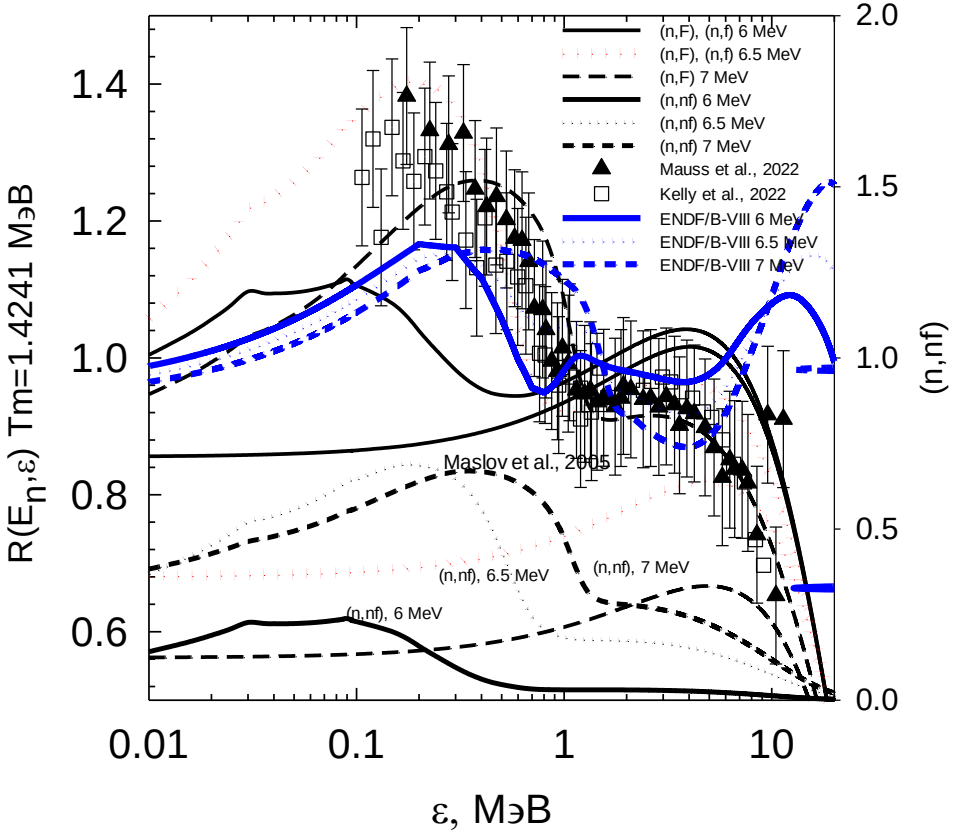

235U(n,F) JENDL-4.0 6,6.5 7 MeV

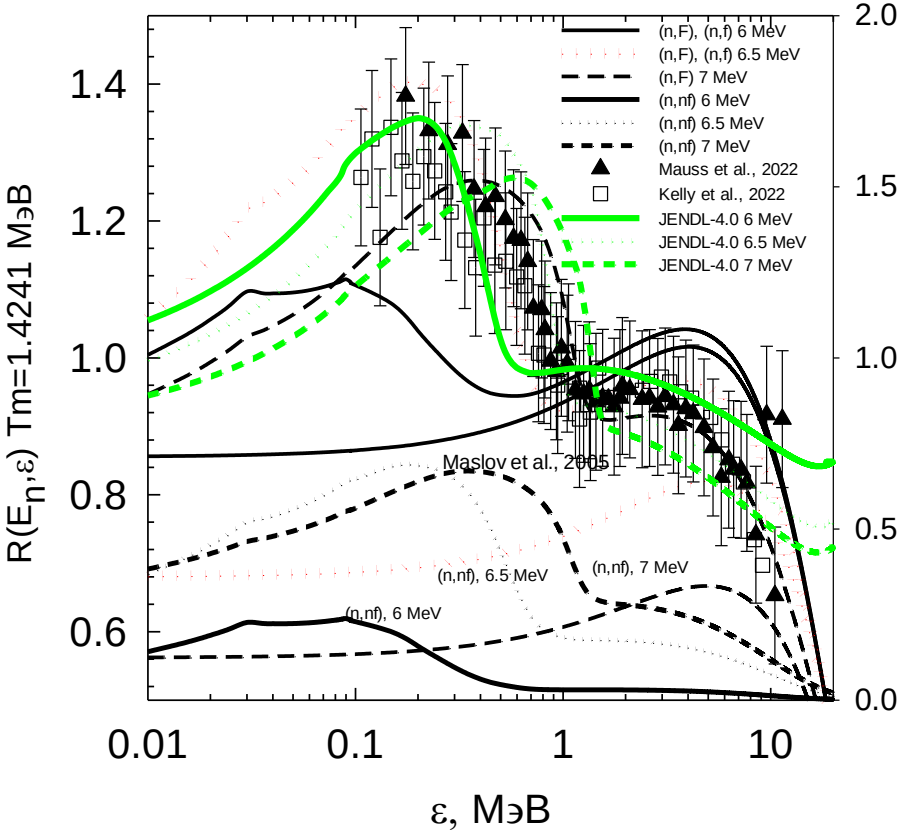

235U(n,F) INDEN 5.5, 6, 7 MeV

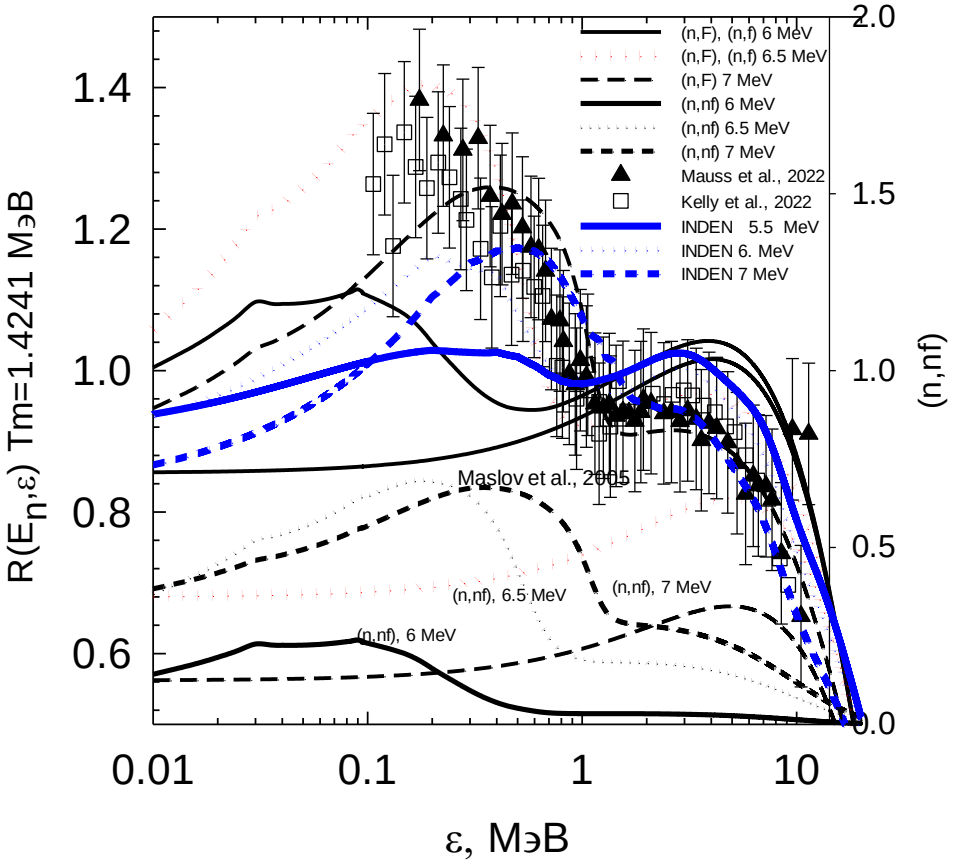

239Pu(n,F) 14.7 MeV

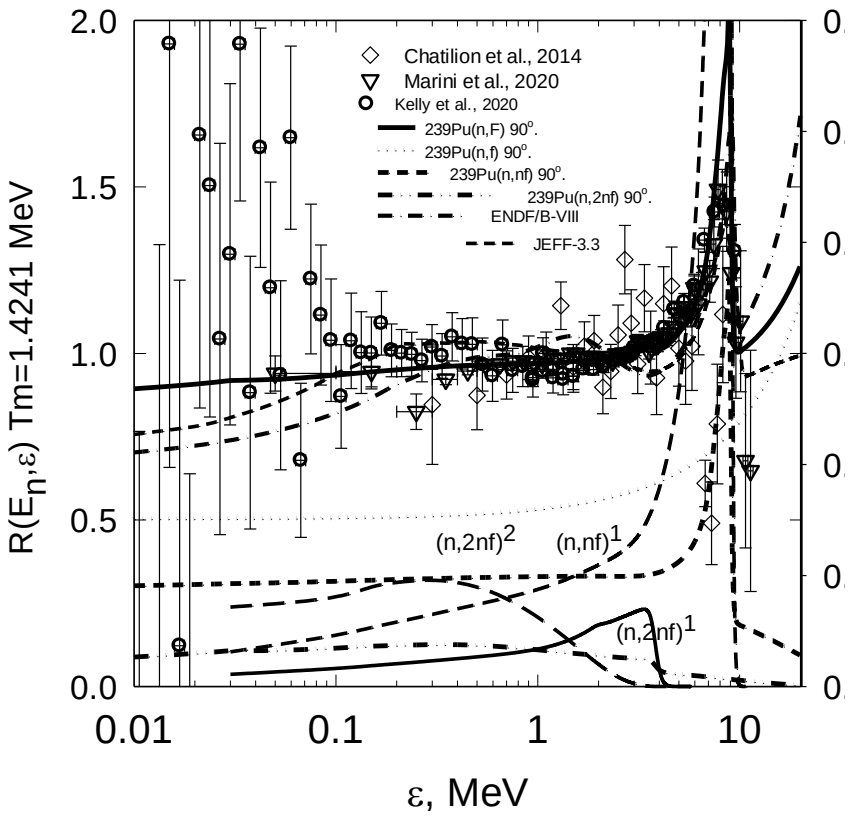

235U(n,F), 14.7 MeV

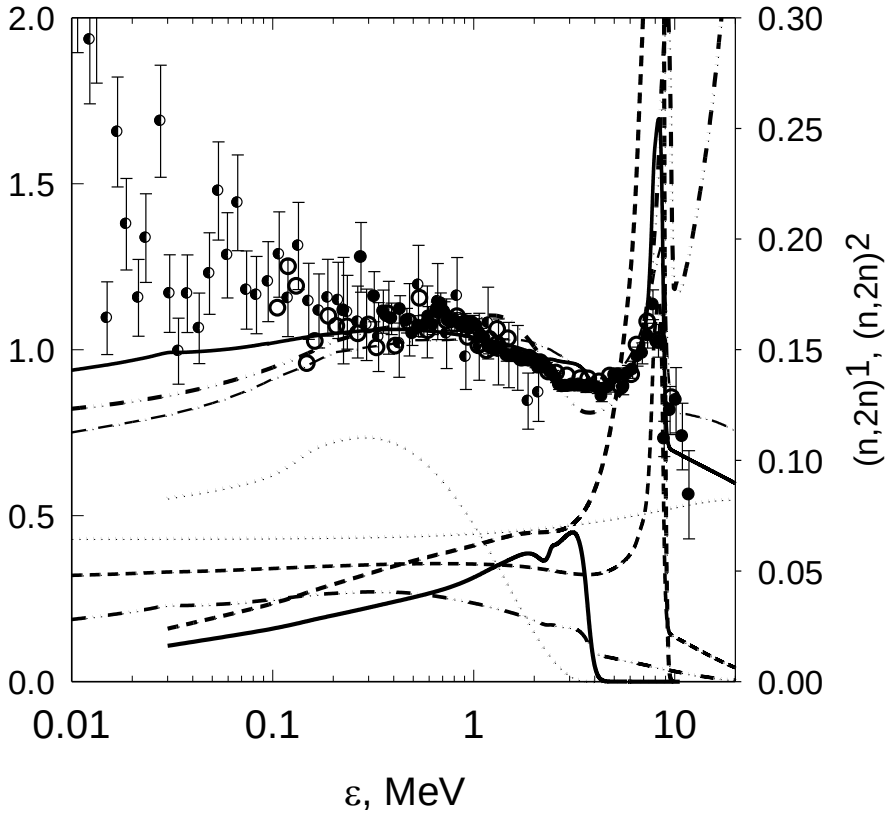

PFNS 239Pu(n,F) 20 MeV

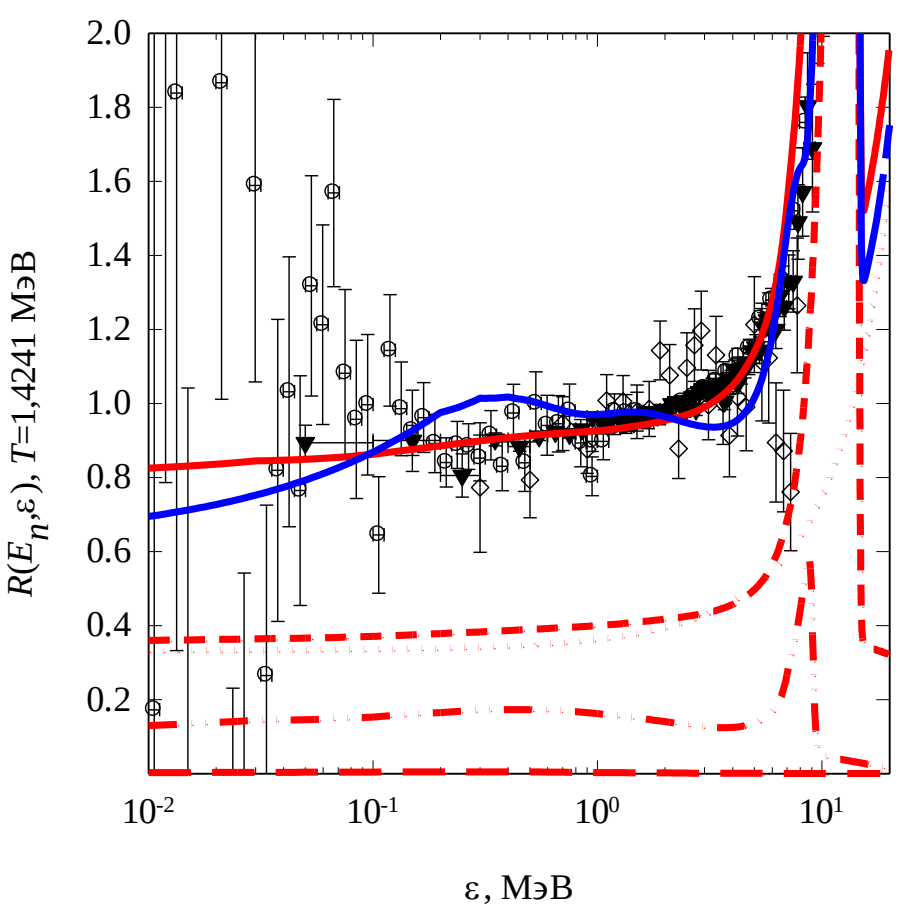

PFNS 235U(n,F) 20 MeV

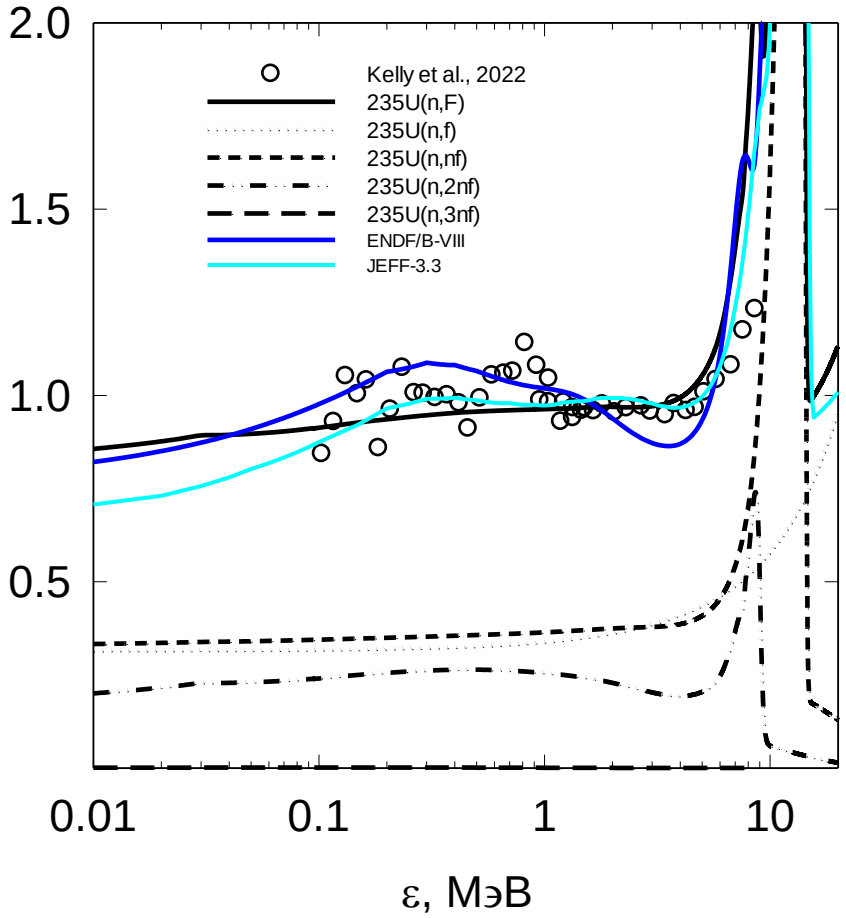

239Pu 14 NES MeV 30 deg

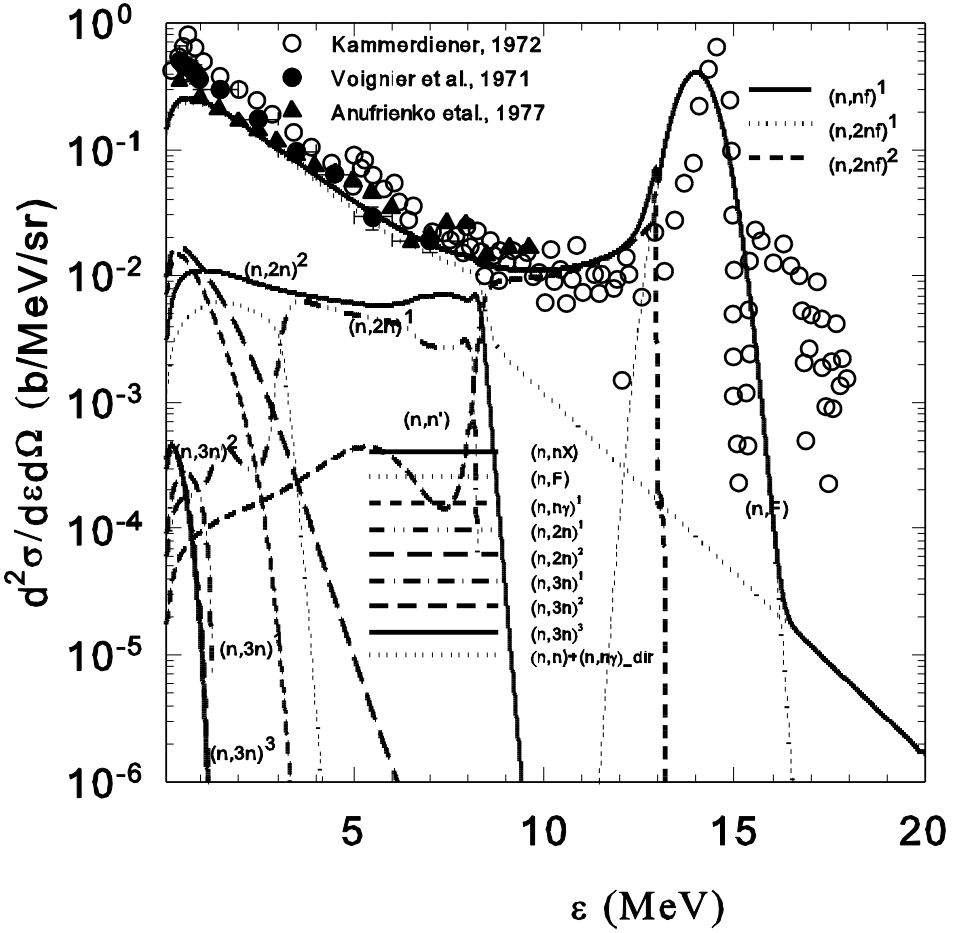

239Pu 14 NES MeV 120 deg

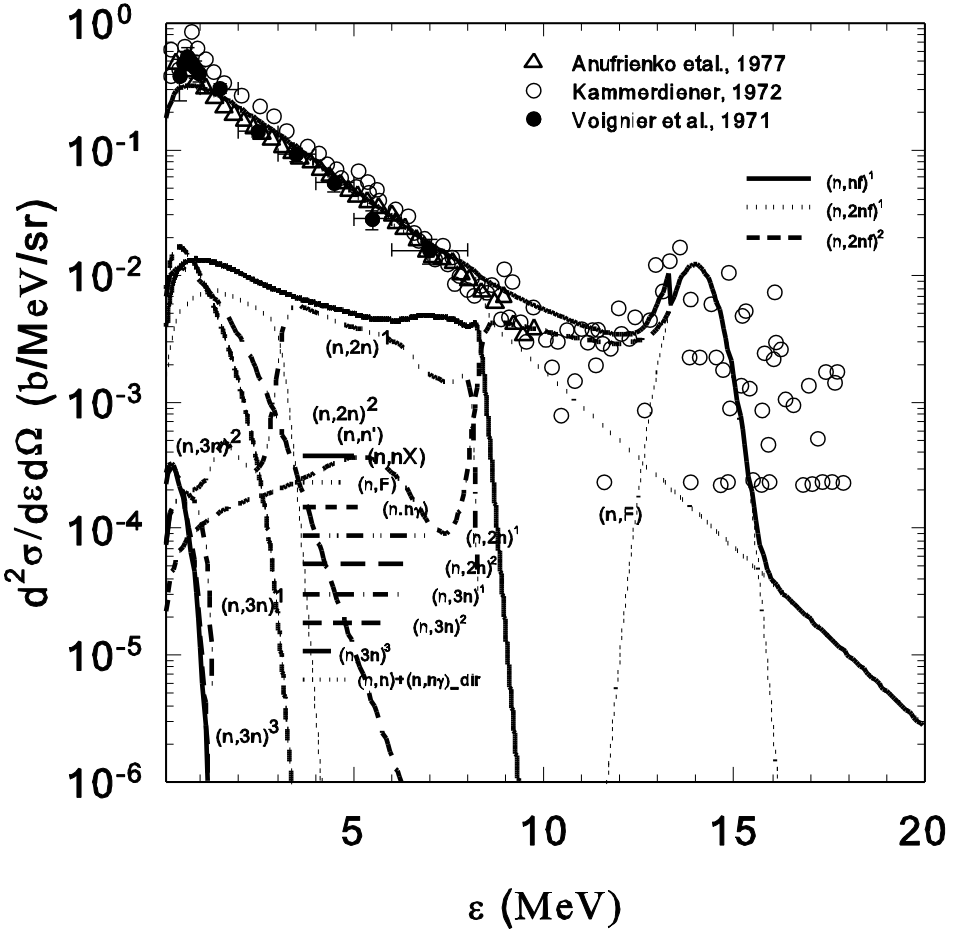

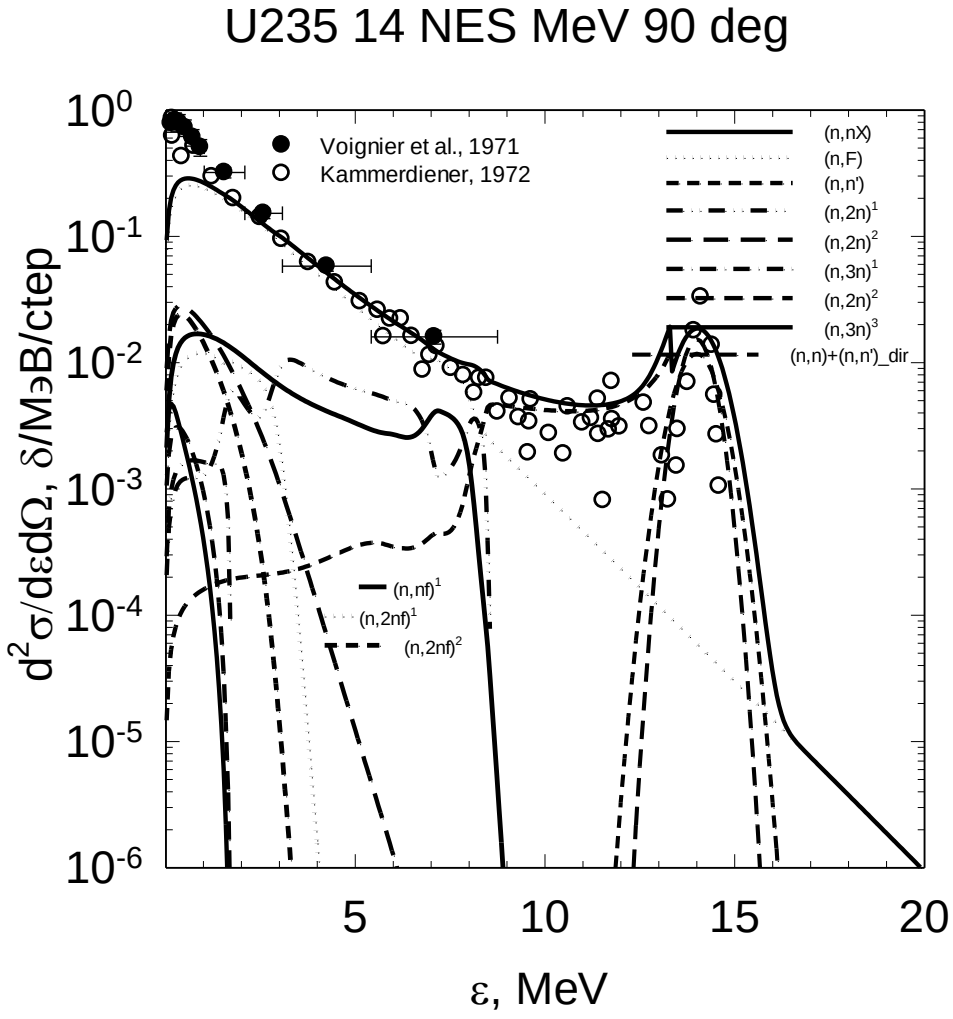
U235 14 NES MeV 90 deg
Voignier et al., 1971
Kammerdiener, 1972
(n,nX)
(n,F)
(n,n')
(n,2n)1
(n,2n)2
(n,3n)1
(n,2n)2
(n,3n)3
(n,n)+(n,n')_dir
(n,nf)1
(n,2nf)1
(n,2nf)2
d2σ/dεdΩ, δ/МэВ/ctep
ε, MeV

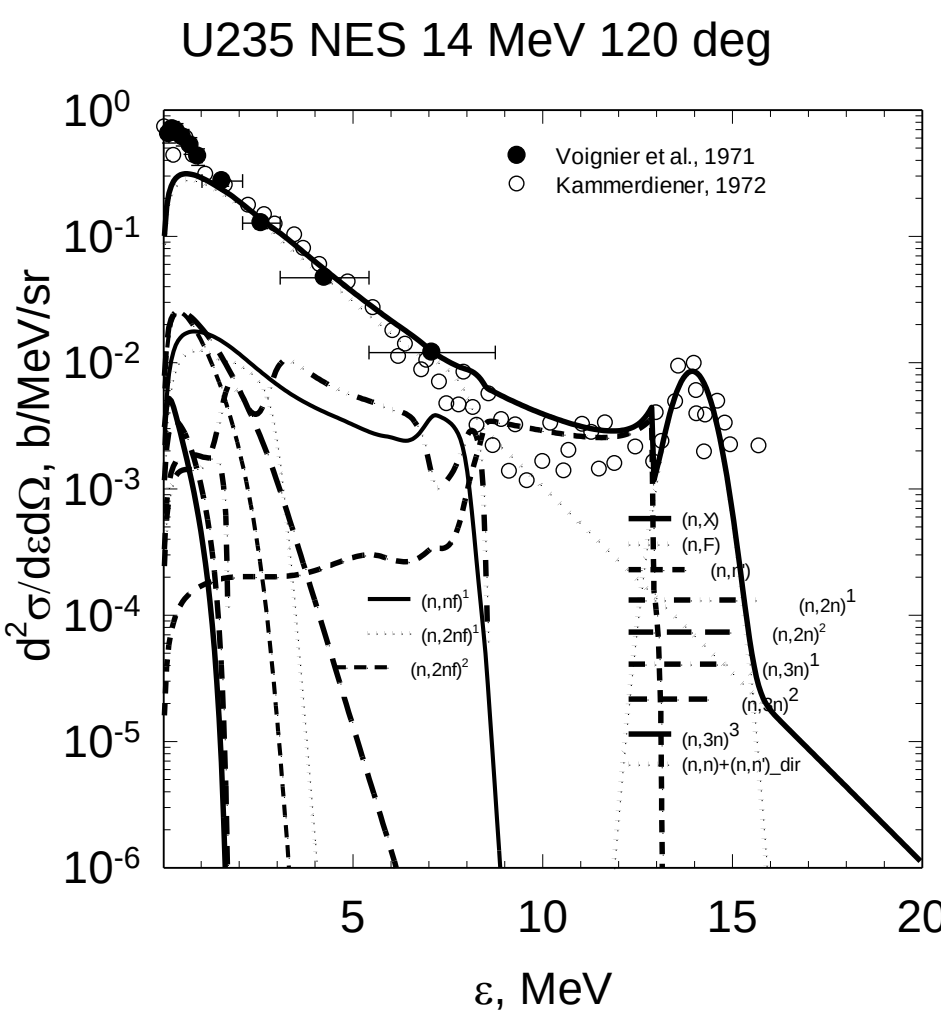
U235 NES 14 MeV 120 deg
Voignier et al., 1971
Kammerdiener, 1972
(n,X)
(n,F)
(n,n')
(n,2n)1
(n,2n)2
(n,3n)1
(n,3n)2
(n,3n)3
(n,n)+(n,n')_dir
(n,nf)1
(n,2nf)1
(n,2nf)2
d2σ/dεdΩ, b/MeV/sr
ε, MeV

235U NES 14 MeV 30 deg

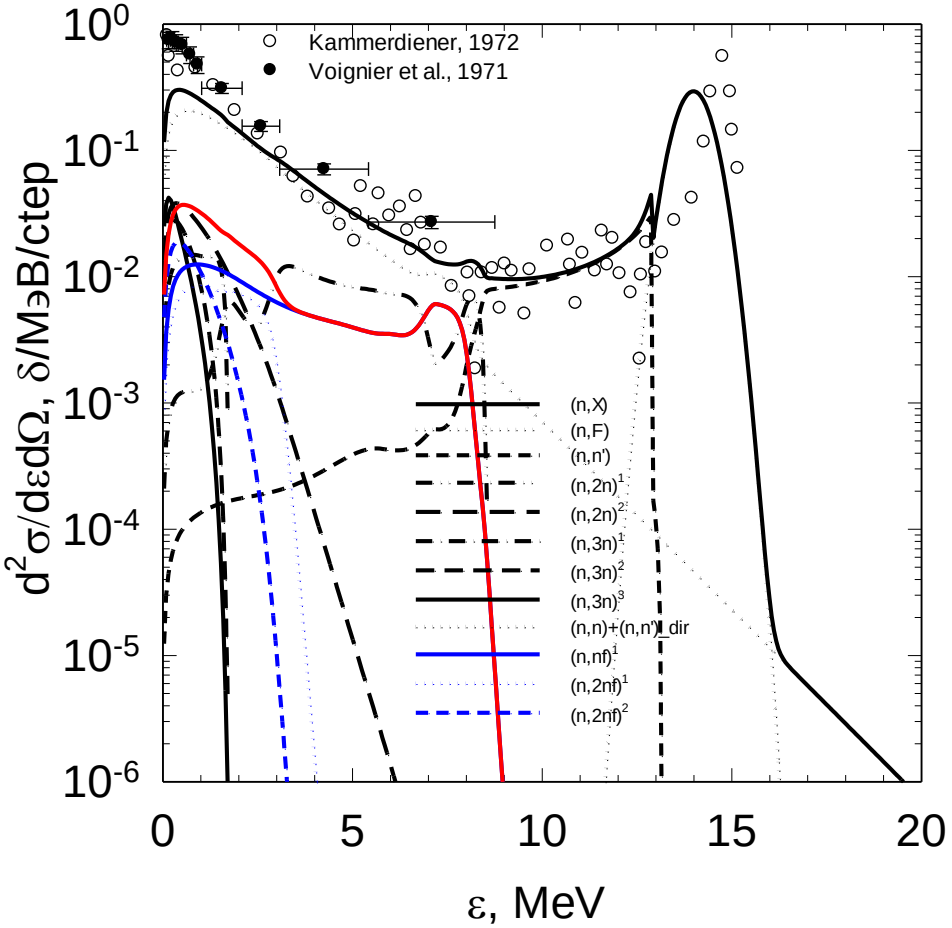

U235 NES 14 MeV 120 deg.

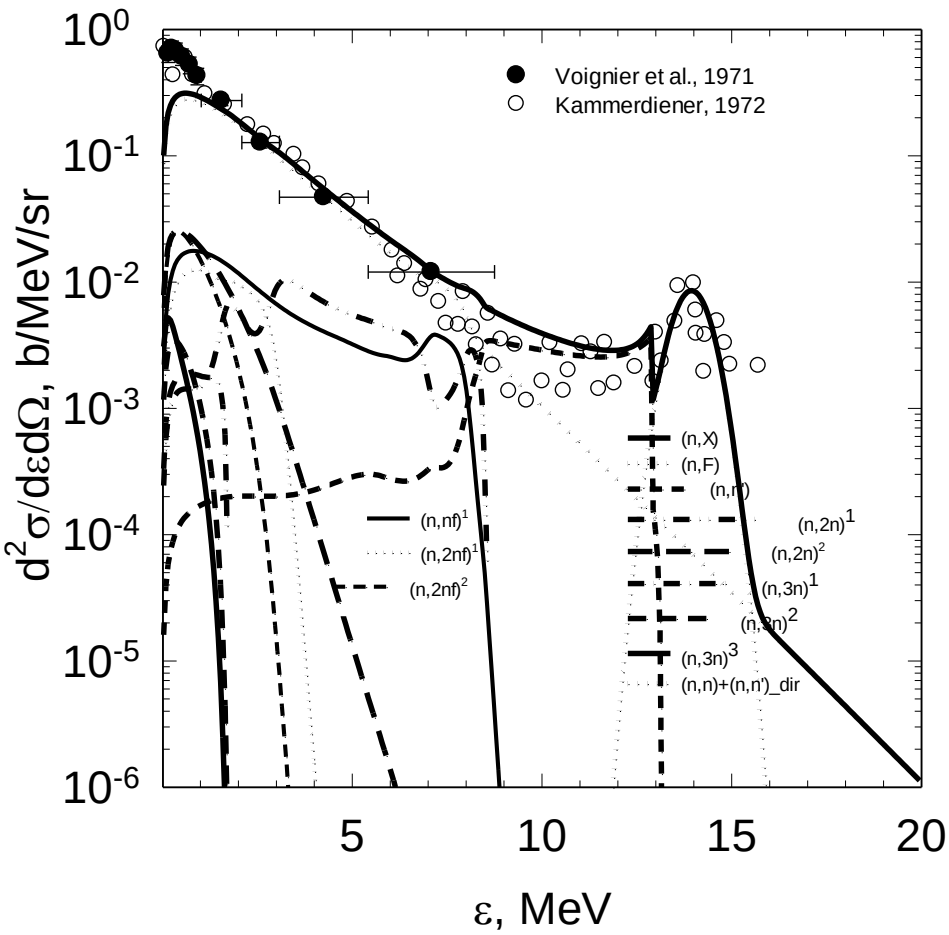

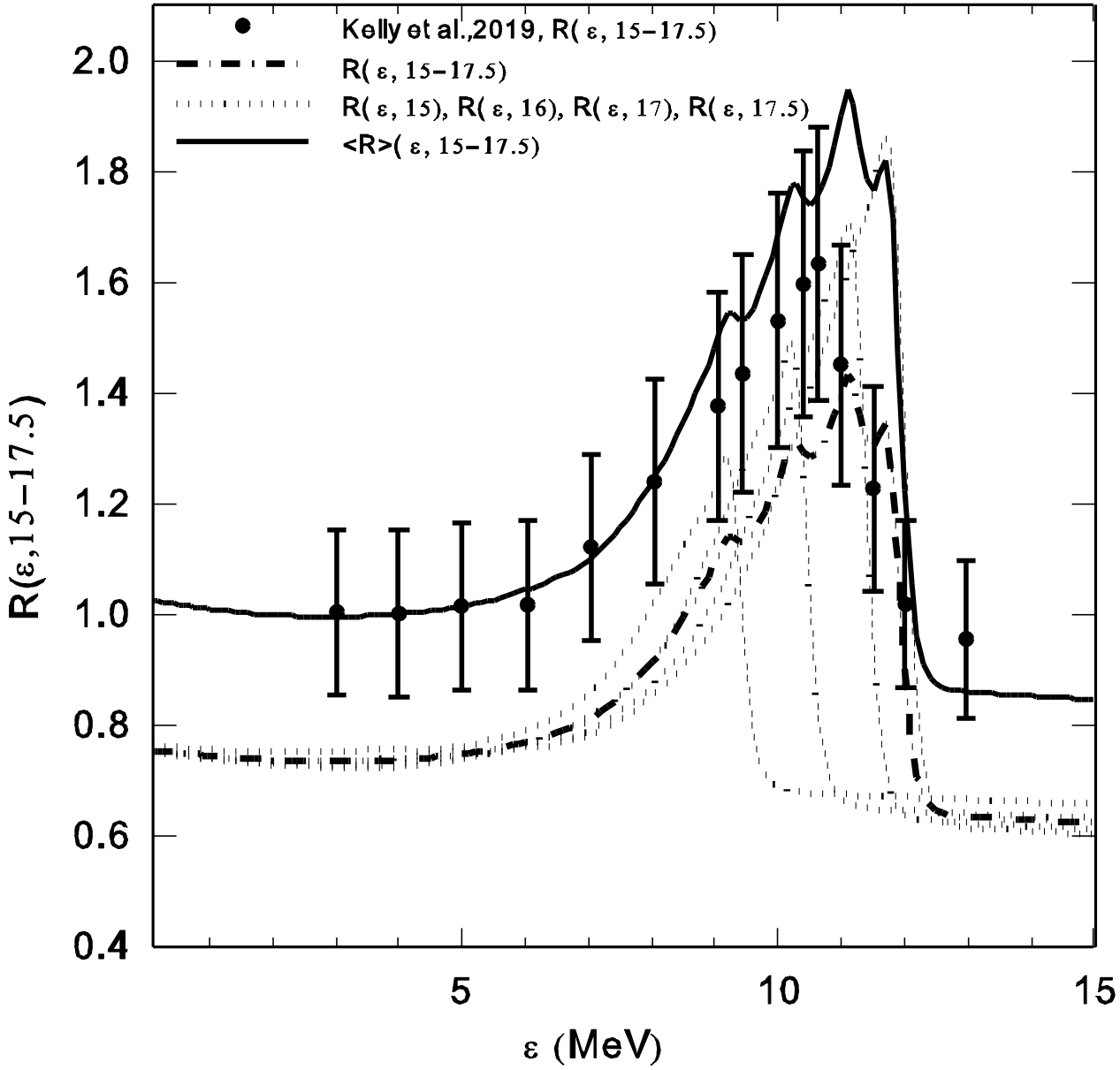
Kelly et al.,2019, R(ε, 15–17.5)
R(ε, 15–17.5)
R(ε, 15), R(ε, 16), R(ε, 17), R(ε, 17.5)
<R>(ε, 15–17.5)
R(ε,15–17.5)
ε (MeV)
2.0
1.8
1.6
1.4
1.2
1.0
0.8
0.6
0.4
5
10
15

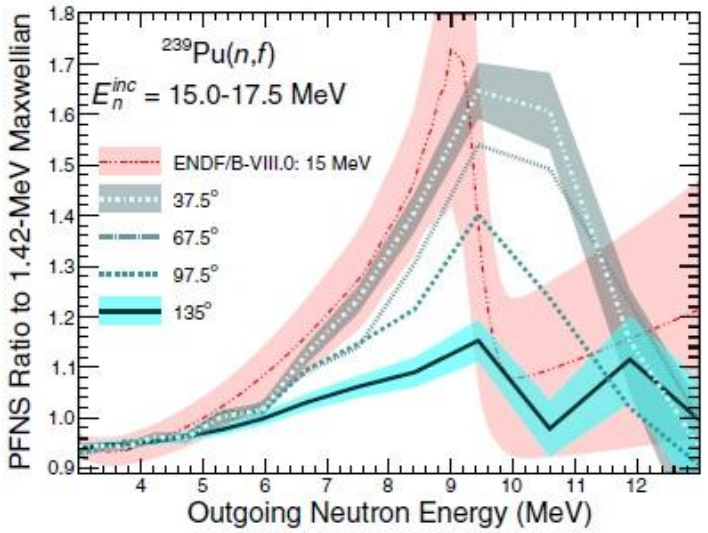

FIG. 3. The angular dependence of the fission neutron spectrum of $^{239}\mathrm{Pu}(n,f)$ is shown. Lines of different styles and shades of blue correspond to different detection angles. The width of the largest and smallest angles represents the statistical uncertainty. The uncertainties for the intermediate angles are not shown but are similar. The ENDF/B-VIII.0 [3] PFNS at $E_n^{\mathrm{inc}} = 15$ MeV is shown as the red dash-triple-dotted line and shaded region, the latter of which represents the evaluation uncertainty. Note that the preequilibrium neutrons are clearly observed even at angles above 90°. All spectra were scaled to have the same integral in the 3–5 MeV outgoing neutron energy range.

the peak of the excess appears to be shifted downward with respect to the incident neutron energy by approximately the fission binding energy (≈6 MeV), as expected for prefission preequilibrium neutron spectra [4]. Figure 3 shows the behavior of the excess observed for an incident energy range of $E_n^{\mathrm{inc}} = 15.0$–$17.5$ MeV as a function of detection angle compared to the ENDF/B-VIII.0 [3] evaluated PFNS for $E_n^{\mathrm{inc}} = 15$ MeV. Note that the ENDF/B-VIII.0 spectra are not differentiated by angle and are assumed to be integrated over all observable angles. The onset energy of this PFNS feature appears consistent with the ENDF/B-VIII.0 prediction, further suggesting that this feature is the preequilibrium prefission component of the PFNS. Additionally, Fig. 3 demonstrates the observation of the expected forward-peaked angular distribution with respect to the momentum direction of the incident neutron beam, which is not to be confused with the orientation of the fission axis.

The strongly anisotropic character of the preequilibrium prefission neutrons implies that the observed PFNS should be harder (i.e., higher average PFNS energy) at forward (small) angles than it is at backward (large) angles once preequilibrium neutron emission is present. This effect is shown in Fig. 4 through the ratio of the average PFNS energy at the minimum detection angle to that of the maximum detection angle for an outgoing PFNS energy range in which largely isotropic postfission neutrons

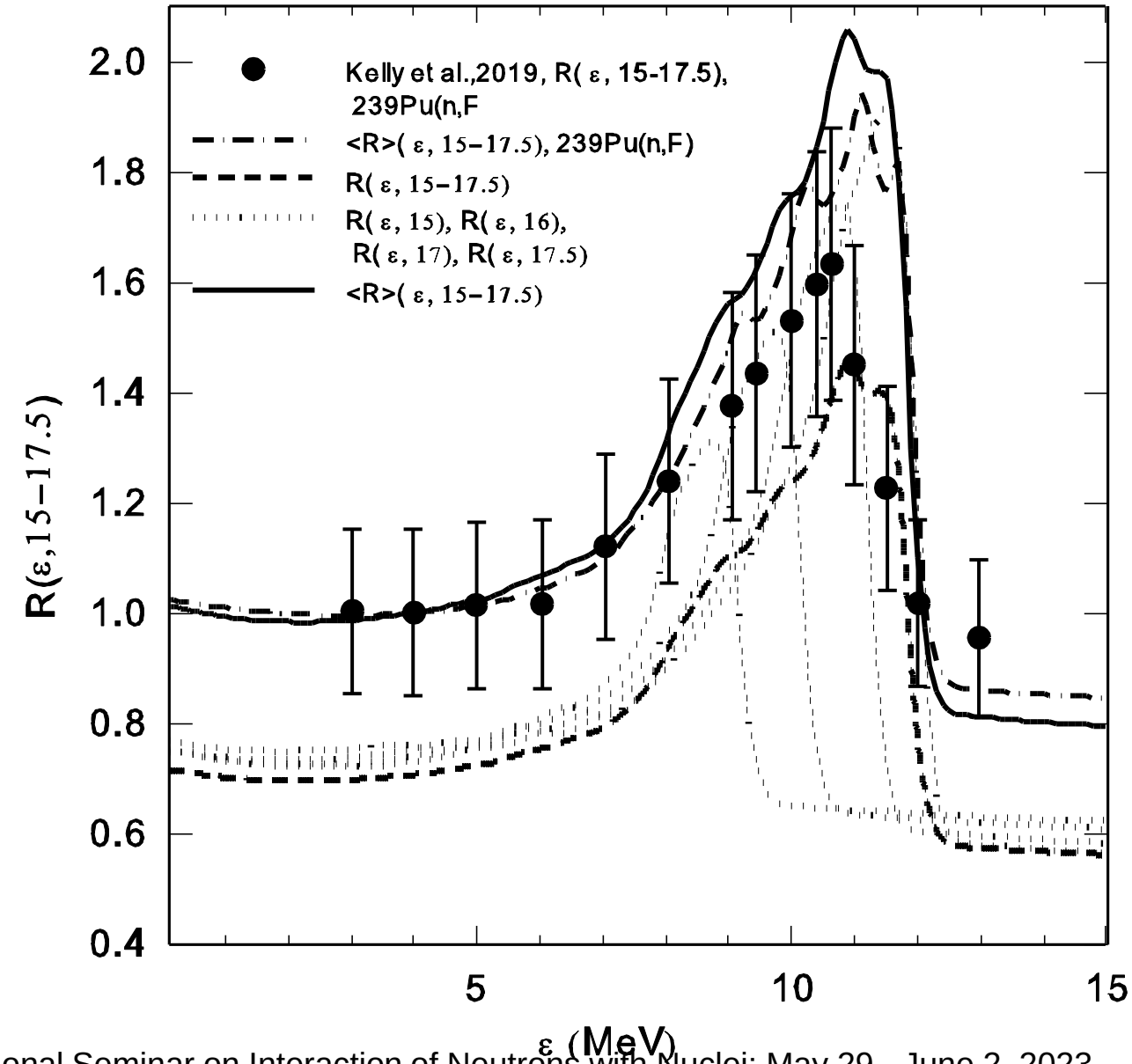
Kelly et al.,2019, R(ε, 15-17.5), 239Pu(n,F
<R>(ε, 15–17.5), 239Pu(n,F)
R(ε, 15–17.5)
R(ε, 15), R(ε, 16), R(ε, 17), R(ε, 17.5)
<R>(ε, 15–17.5)
R(ε,15–17.5)
ε (MeV)
2.0
1.8
1.6
1.4
1.2
1.0
0.8
0.6
0.4
5
10
15

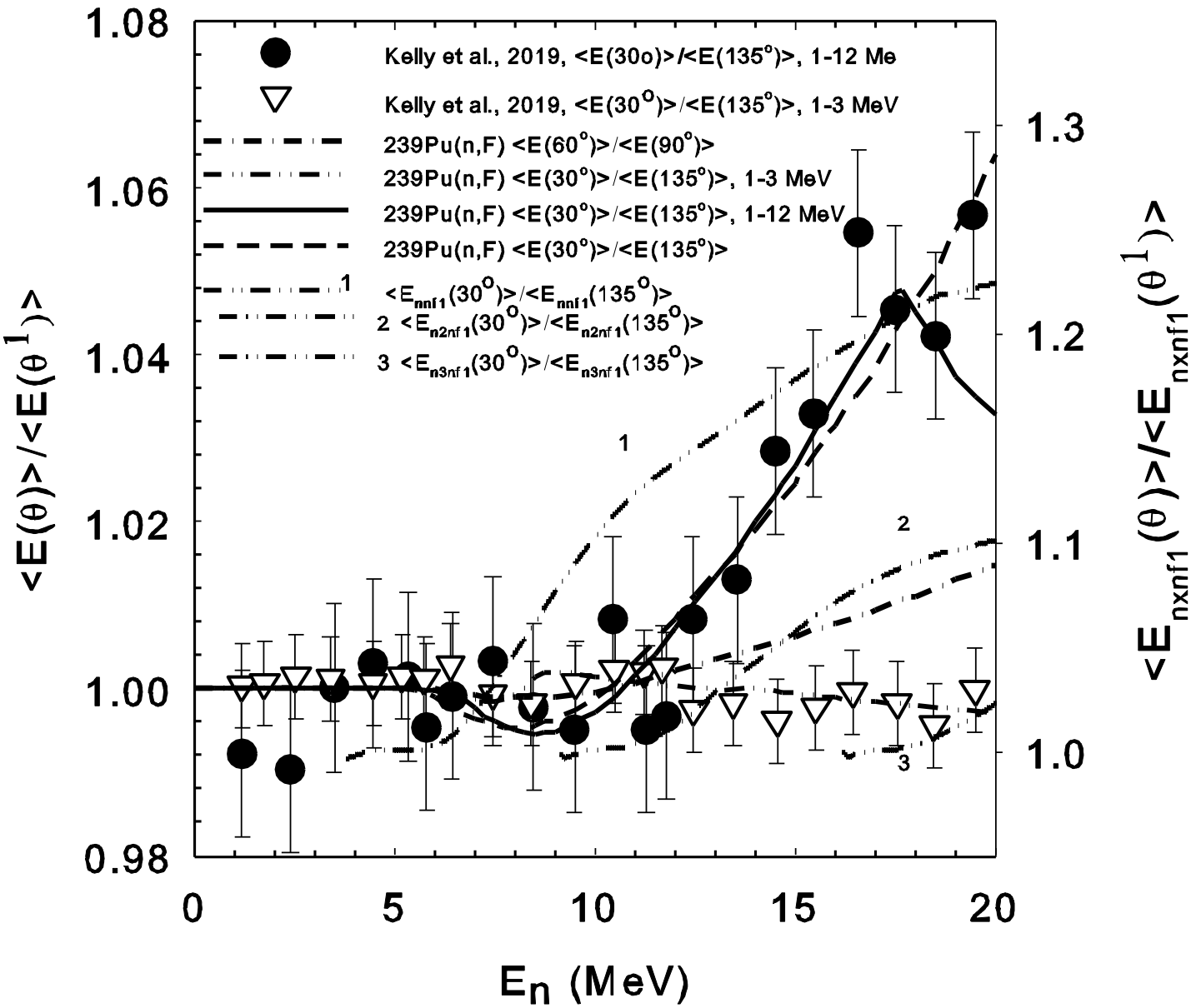
Kelly et al., 2019, <E(30o)>/<E(135°)>, 1-12 Me
Kelly et al., 2019, <E(30°)>/<E(135°)>, 1-3 MeV
239Pu(n,F) <E(60°)>/<E(90°)>
239Pu(n,F) <E(30°)>/<E(135°)>, 1-3 MeV
239Pu(n,F) <E(30°)>/<E(135°)>, 1-12 MeV
239Pu(n,F) <E(30°)>/<E(135°)>
1 <E_nnf1(30°)>/<E_nnf1(135°)>
2 <E_n2nf1(30°)>/<E_n2nf1(135°)>
3 <E_n3nf1(30°)>/<E_n3nf1(135°)>
<E(θ)>/<E(θ^1)>
<E_nxnf1(θ)>/<E_nxnf1(θ^1)>
E_n (MeV)
1.08
1.06
1.04
1.02
1.00
0.98
1.3
1.2
1.1
1.0
0
5
10
15
20

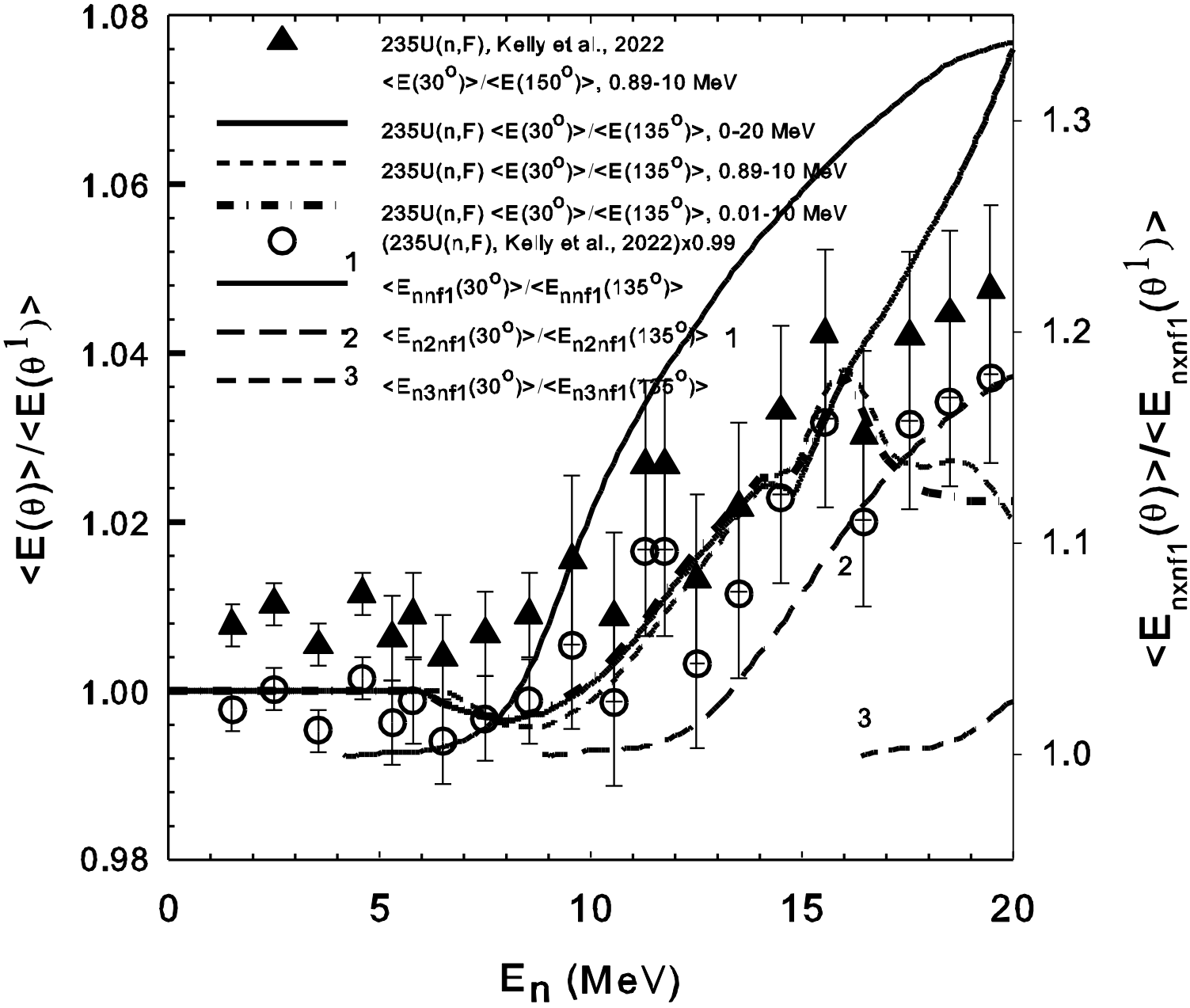
235U(n,F), Kelly et al., 2022
<E(30°)>/<E(150°)>, 0.89-10 MeV
235U(n,F) <E(30°)>/<E(135°)>, 0-20 MeV
235U(n,F) <E(30°)>/<E(135°)>, 0.89-10 MeV
235U(n,F) <E(30°)>/<E(135°)>, 0.01-10 MeV
(235U(n,F), Kelly et al., 2022)x0.99
1
<E_nnf1(30°)>/<E_nnf1(135°)>
2
<E_n2nf1(30°)>/<E_n2nf1(135°)>
3
<E_n3nf1(30°)>/<E_n3nf1(135°)>
<E(θ)>/<E(θ^1)>
<E_nxnf1(θ)>/<E_nxnf1(θ^1)>
E_n (MeV)
1.08
1.06
1.04
1.02
1.00
0.98
1.3
1.2
1.1
1.0
0
5
10
15
20

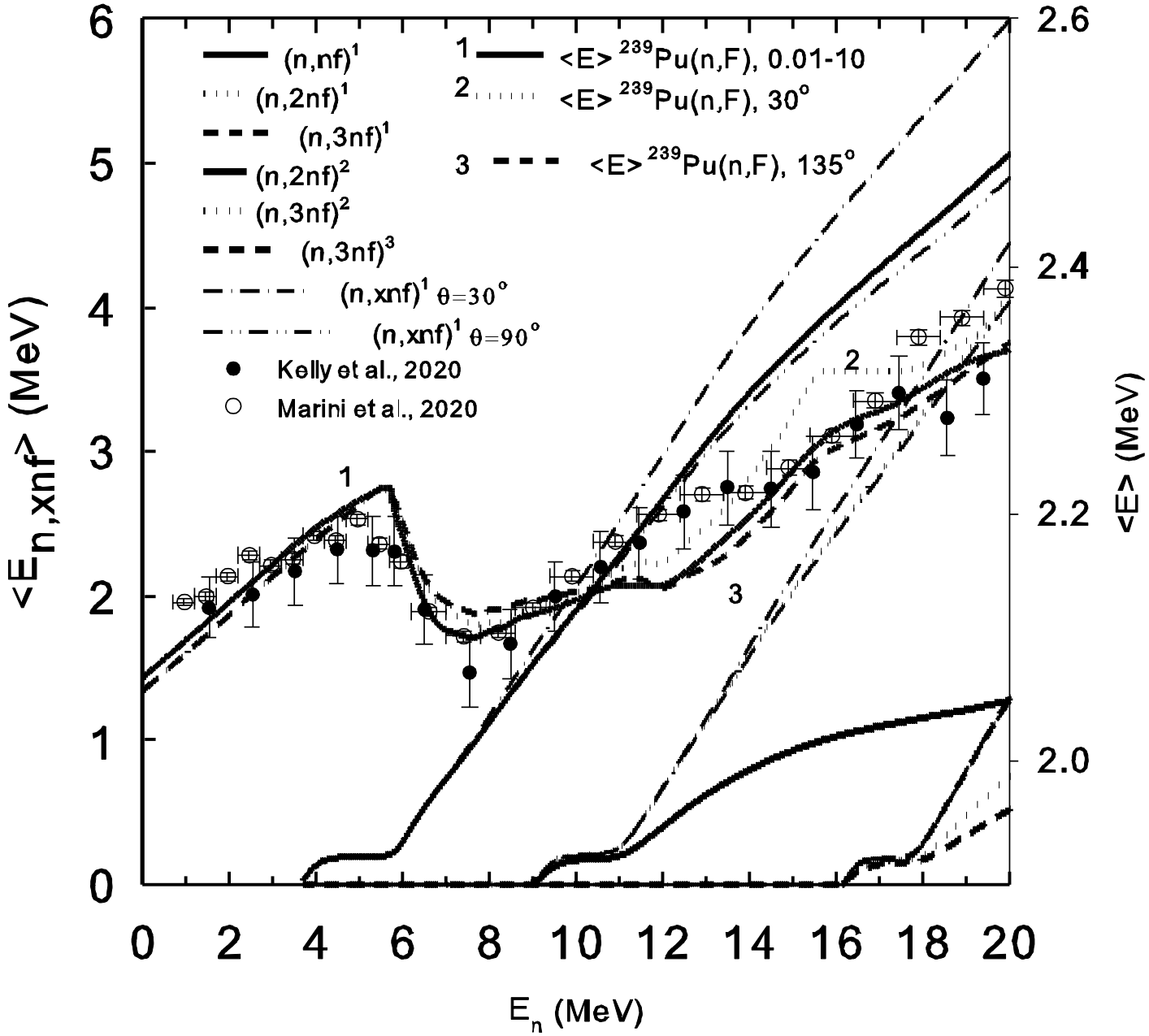
(n,nf)1
(n,2nf)1
(n,3nf)1
(n,2nf)2
(n,3nf)2
(n,3nf)3
(n,xnf)1 θ=30°
(n,xnf)1 θ=90°
Kelly et al., 2020
Marini et al., 2020
1 <E> 239Pu(n,F), 0.01-10
2 <E> 239Pu(n,F), 30°
3 <E> 239Pu(n,F), 135°
<En,xnf> (MeV)
<E> (MeV)
En (MeV)
0
1
2
3
4
5
6
2.0
2.2
2.4
2.6
0
2
4
6
8
10
12
14
16
18
20

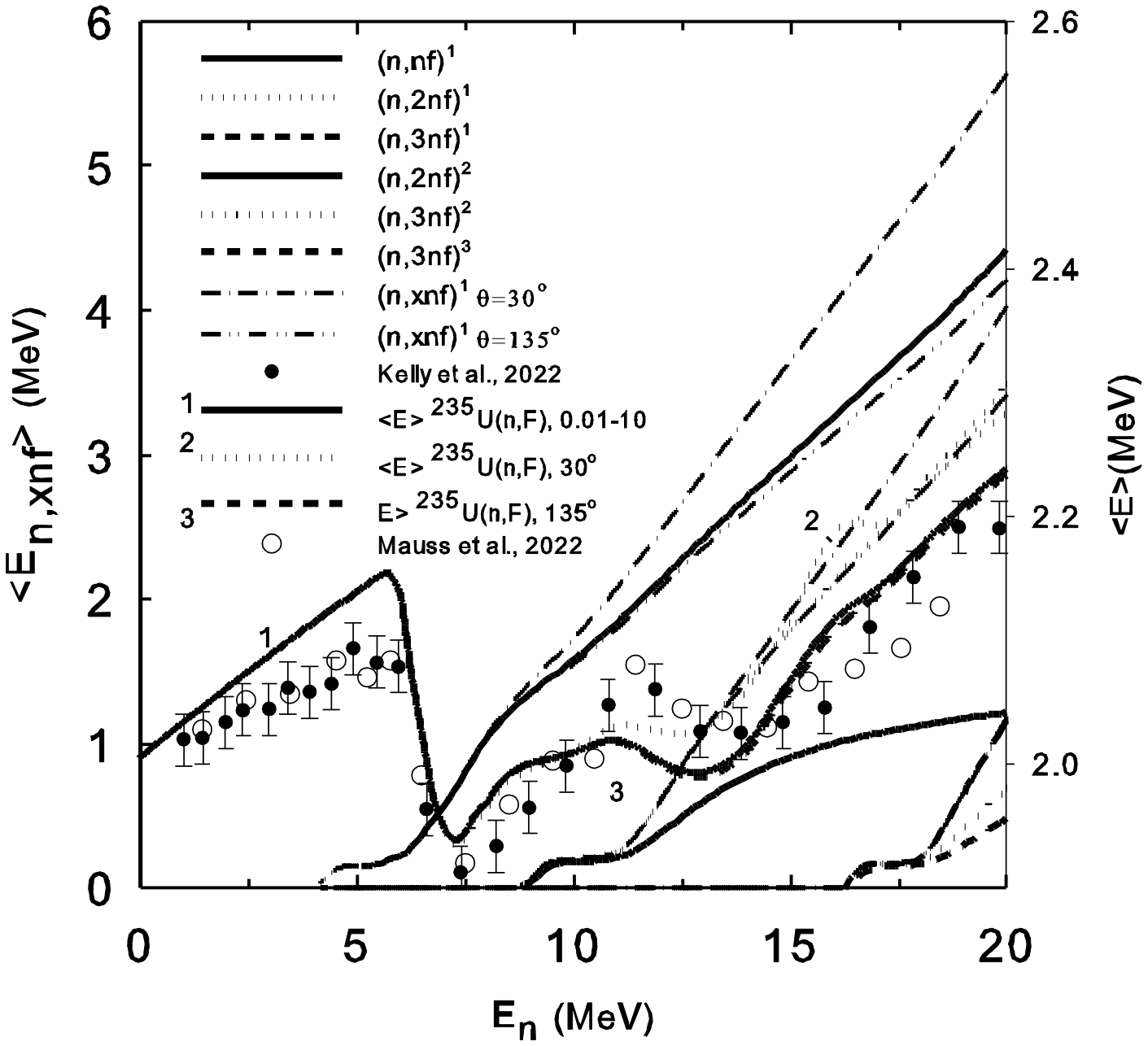
(n,nf)1
(n,2nf)1
(n,3nf)1
(n,2nf)2
(n,3nf)2
(n,3nf)3
(n,xnf)1 θ=30°
(n,xnf)1 θ=135°
Kelly et al., 2022
1 <E> 235U(n,F), 0.01-10
2 <E> 235U(n,F), 30°
3 E> 235U(n,F), 135°
Mauss et al., 2022
<En,xnf> (MeV)
<E>(MeV)
En (MeV)
0
1
2
3
4
5
6
2.0
2.2
2.4
2.6
0
5
10
15
20

TKE 239Pu(n,F)

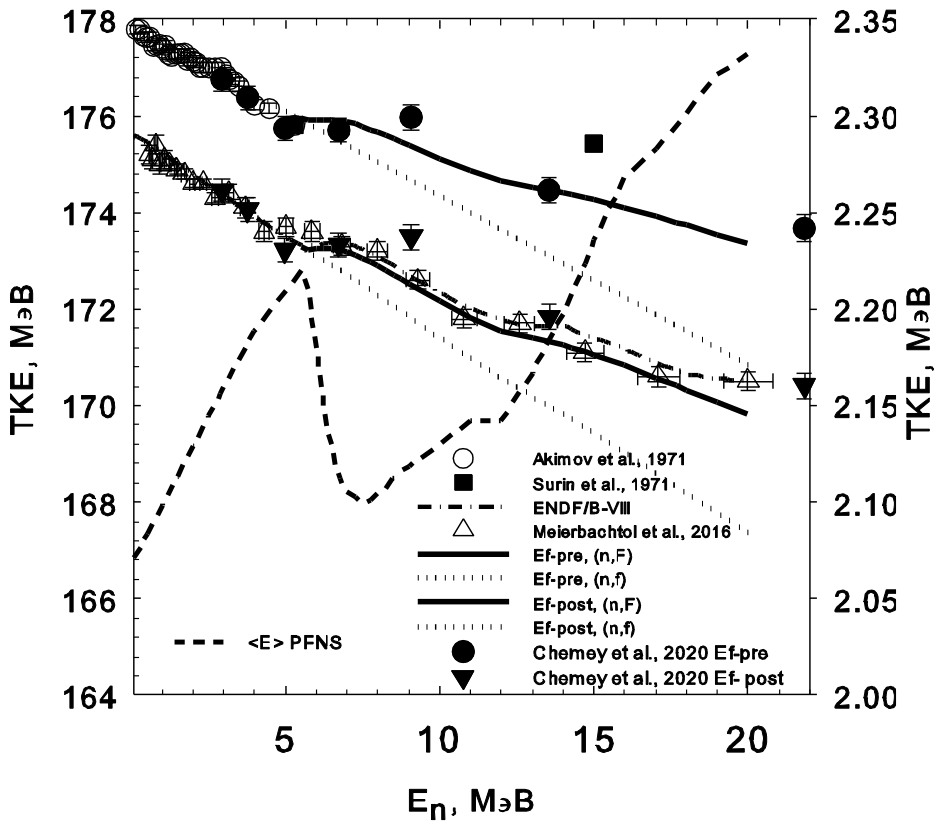

TKE 235U(n,F)

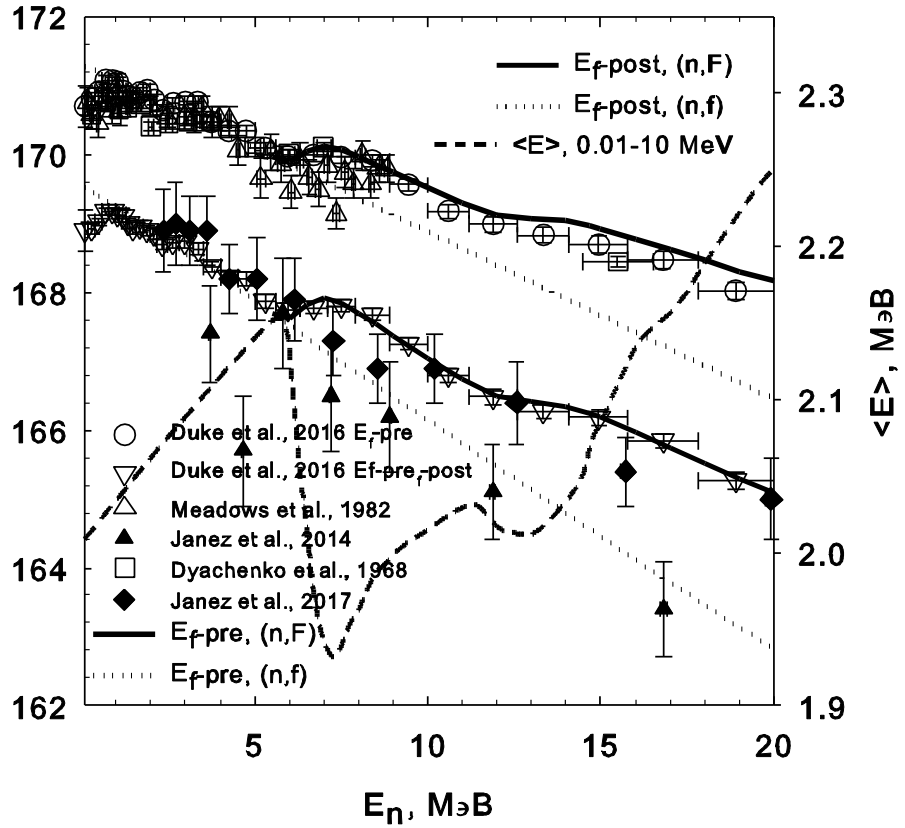

TKE vis PFNS <E> 232Th(n,F)

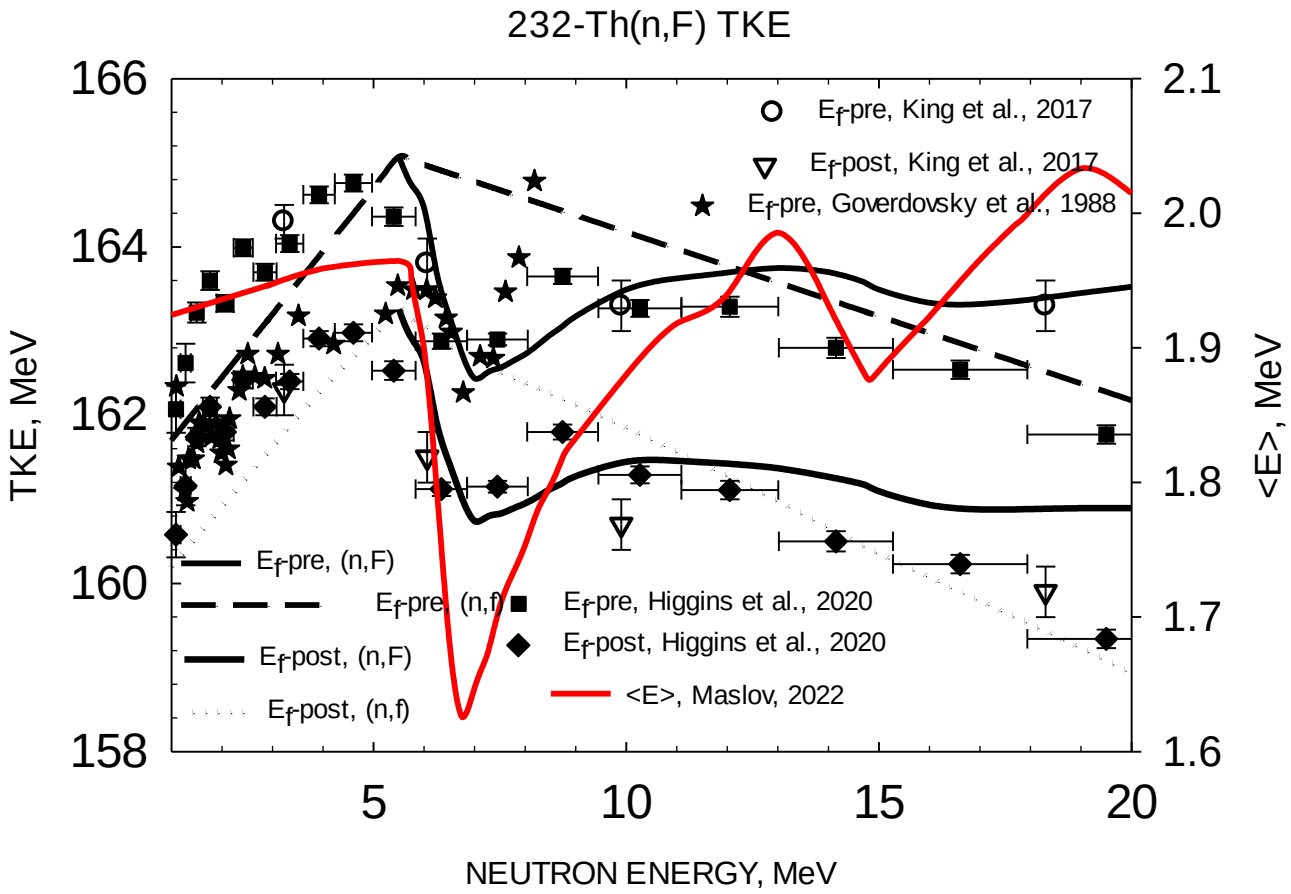

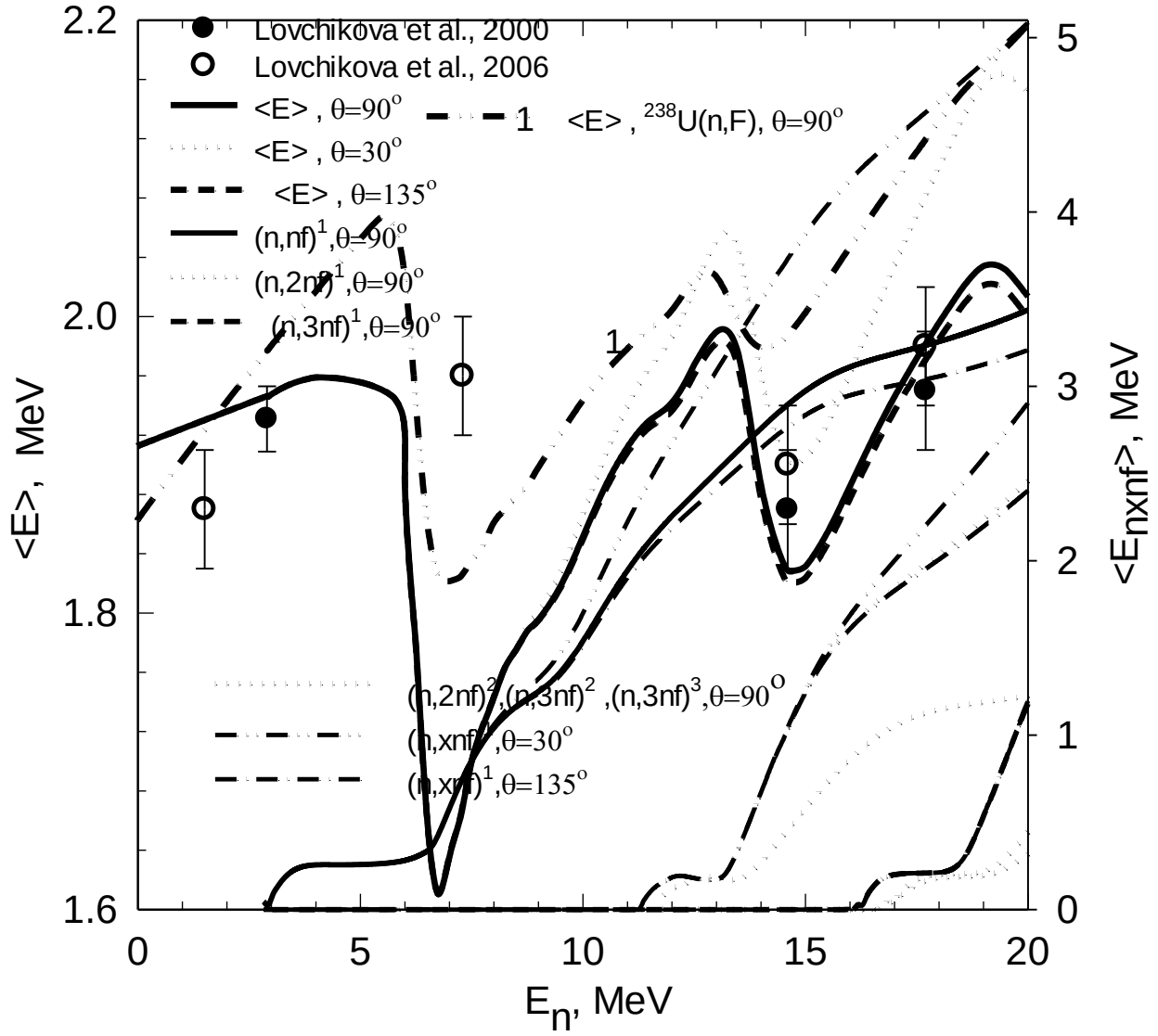
Lovchikova et al., 2000
Lovchikova et al., 2006
<E> , θ=90°
<E> , θ=30°
<E> , θ=135°
(n,nf)1,θ=90°
(n,2nf)1,θ=90°
(n,3nf)1,θ=90°
1
<E> , 238U(n,F), θ=90°
(n,2nf)2,(n,3nf)2 ,(n,3nf)3,θ=90°
(n,xnf)1,θ=30°
(n,xnf)1,θ=135°
<E>, MeV
<EnxnF>, MeV
En, MeV
2.2
2.0
1.8
1.6
0
5
10
15
20
0
1
2
3
4
5

Conclusions

Angular dependence of first $(n,nX)^1$ emission $W(\theta)$ being included.

Average energy of $(n,nf)^1$ neutrons depends on the emission angle θ

Fission cross section, prompt neutron number and total kinetic energy depend on θ as well

Exclusive neutron spectra $(n,xnf)^{1,..x}$ at θ~90^o are consistent with ^{235}U(n,F)(^{235}U(n,xn)) and ^{239}Pu(n,F)(^{239}Pu(n,xn)) css within E_n~0.01–20 MeV

Exclusive neutron spectra of $(n,xnf)^{1,..x}$, $(n,n\gamma)$ and $(n,xn)^{1,..x}$ are of Hauser-Feshbach formalism

Conclusions

Approximation obtained for W(θ) fits the measured NES at 14 MeV.

The correlation of angular dependence of (n,xnf)[1] neutron emission with emissive fission (n,xnf) contribution to the observed fission cross section and angular anisotropy of NES is established.

The ratios of mean PFNS energies <E> for forward and backward emission of ^{235}U(n,xnf) and ^{239}Pu(n,xnf) pre-fission neutrons are consistent with measured data.

Conclusions

In **^{239}Pu(n,xnf)$^{1,..x}$ and ^{235}U(n,xnf)$^{1,..x}$ PFNS** demonstrate different responses to forward and backward (n,xnf)^{1} neutrons emission with respect to the incident neutron momentum

In **^{232}Th(n,xnf)$^{1,..x}$ and ^{232}Th(n,F) PFNS** the strongest response to forward and backward (n,xnf)^{1} neutrons emission with respect to the incident neutron momentum is predicted